European Journal of Medicinal Chemistry 275 (2024) 116567

Contents lists available at ScienceDirect

European Journal of Medicinal Chemistry

journal homepage: www.elsevier.com/locate/ejmech

Research paper

A chemical modification of a peroxisome proliferator-activated receptor pan agonist produced a shift to a new dual alpha/gamma partial agonist endowed with mitochondrial pyruvate carrier inhibition and antidiabetic properties

Antonio Laghezza [a,1], Carmen Cerchia [b,1], Massimo Genovese [c], Roberta Montanari [d], Davide Capelli [d], Judith Wackerlig [e], Stefan Simic [e], Emanuele Falbo [b], Lucia Pecora [c], Rosalba Leuci [a], Leonardo Brunetti [a], Luca Piemontese [a], Paolo Tortorella [a], Abanish Biswas [f], Ravi Pratap Singh [f], Suhas Tambe [g], C.A. Sudeep [h], Ashok Kumar Pattnaik [f], Venkatesan Jayaprakash [f], Paolo Paoli [c], Antonio Lavecchia [b,**], Fulvio Loiodice [a,*]

[a] Dipartimento Farmacia-Scienze del Farmaco, Università degli Studi di Bari "Aldo Moro", via Orabona 4, 70125, Bari, Italy
[b] Dipartimento di Farmacia, "Drug Discovery" Laboratory, Università degli Studi di Napoli "Federico II", via D. Montesano 49, 80131, Napoli, Italy
[c] Dipartimento di Scienze Biomediche Sperimentali e Cliniche, Sezione di Scienze Biochimiche, Università degli Studi di Firenze, Viale Morgagni 50, 50134, Firenze, Italy
[d] Istituto di Cristallografia, Consiglio Nazionale delle Ricerche, Montelibretti, 00015 Monterotondo Stazione, Roma, Italy
[e] Department of Pharmaceutical Sciences, Faculty of Life Sciences, University of Vienna, 1090, Vienna, Austria
[f] Department of Pharmaceutical Sciences & Technology, Birla Institute of Technology, Mesra, Ranchi, Jharkhand, 835215, India
[g] Adgyl Lifescience Private Ltd., Bengaluru, 560058, India
[h] Bioanalytical Section, Eurofins Advinus Biopharma Services India Pvt Ltd., Bengaluru, 560058, India

ARTICLE INFO

Keywords:
PPAR dual-agonist
Crystallographic studies
Docking experiments
MPC inhibition
Anti-steatotic effects
Glucose uptake

ABSTRACT

New analogs of the PPAR pan agonist AL29-26 encompassed ligand (*S*)-**7** showing potent activation of PPARα and -γ subtypes as a partial agonist. In vitro experiments and docking studies in the presence of PPAR antagonists were performed to help interpretation of biological data and investigate the main interactions at the binding sites. Further in vitro experiments showed that (*S*)-**7** induced anti-steatotic effects and enhancement of the glucose uptake. This latter effect could be partially ascribed to a significant inhibition of the mitochondrial pyruvate carrier demonstrating that (*S*)-**7** also acted through insulin-independent mechanisms. In vivo experiments showed that this compound reduced blood glucose and lipid levels in a diabetic mice model displaying no toxicity on bone, kidney, and liver. To our knowledge, this is the first example of dual PPARα/γ partial agonist showing these combined effects representing, therefore, the potential lead of new drugs for treatment of dyslipidemic type 2 diabetes.

1. Introduction

Peroxisome proliferator-activated receptors (PPARs) are members of the nuclear receptor superfamily that control important metabolic functions in the body, mainly implicated in lipid and glucose homeostasis, insulin sensitivity, and energetic metabolism. For this reason, they have been considered suitable targets for the treatment of metabolic disorders comprising obesity, type 2 diabetes mellitus (T2DM), dyslipidemia, and hypertension [1,2]. This family includes three receptor subtypes, namely PPARα, PPARγ, and PPARδ (or β/δ),

Abbreviations: PPAR, peroxisome proliferator-activated receptor; LBD, ligand binding domain; TZDs, thiazolidinediones; NBDG, nitrobenzofurazan-deoxy-glucose; MPC, mitochondrial pyruvate carrier; ECAR, extracellular acidification rate; OCR, oxygen consumption rate.

* Corresponding author. Dipartimento di Farmacia-Scienze del Farmaco, Università degli Studi di Bari "Aldo Moro", Via E. Orabona 4, 70125, Bari, Italy.
** Corresponding author.
E-mail addresses: antonio.lavecchia@unina.it (A. Lavecchia), fulvio.loiodice@uniba.it (F. Loiodice).
[1] These Authors contributed equally to this work.

https://doi.org/10.1016/j.ejmech.2024.116567
Received 12 April 2024; Received in revised form 23 May 2024; Accepted 1 June 2024
Available online 9 June 2024

which differ for their tissue distribution, ligand specificity, and also for the downstream effects of their activation.

PPARα is expressed in tissues with a high rate of fatty acid oxidation, such as skeletal muscle, liver, heart, kidney and brown adipose tissue, and modulates lipid metabolism and inflammation [3]. It is the molecular target of fibrates, a class of drugs that lower plasma triglycerides and increase HDL cholesterol levels in humans [4,5]. Furthermore, PPARα agonists can increase the stability of atherosclerotic plaques, reduce the risk of atherothrombosis, and reduce hepatic fat accumulation leading to nonalcoholic steatohepatitis/fatty liver disease (NASH/NAFLD) [6,7].

PPARγ is mainly expressed in adipose tissue, where it induces lipogenesis and fat storage, and in skeletal muscle, where it improves insulin sensitivity [8]. Thiazolidinediones (TZDs), including rosiglitazone and pioglitazone, have been demonstrated to behave as PPARγ full agonists, which activate PPARγ leading to a wide spectrum of genes expression changes involved in insulin sensitizing activity [9]. They are the only clinically available agents controlling hyperglycemia by improving insulin resistance, which is regarded as hallmark and early etiologic basis for T2DM.

PPARδ, the less understood PPAR subtype, is more ubiquitously expressed; it is involved in metabolic disorders, inflammation, and angiogenesis. PPARδ agonists have not yet reached the market, but some of them are being investigated for a possible therapeutic usefulness in the treatment of metabolic disorders, inflammation, and angiogenesis [10].

Recent studies have demonstrated that the full activation of these receptors, especially PPARγ, is associated with unwanted effects. Commonly reported adverse events for fibrates include elevations in markers for cardiovascular disease, renal disease, and liver dysfunction [5,6,11], whereas recent studies have demonstrated that the use of TZDs is associated with unwanted effects, such as weight gain, fluid retention, increased incidence of cardiovascular events, and bone fractures [12–15].

To overcome these issues, new research strategies have been undertaken with the aim to obtain new PPAR ligands with reduced side effects and improved beneficial effects. One of these strategies consists in the synthesis of PPARα/γ dual or PPARα/γ/δ pan-agonists, which beneficially alter carbohydrate and lipid metabolism in a coordinated manner. In fact, these compounds would combine the agonistic activities toward different PPAR subtypes in a single ligand but with a balanced activation profile. This strategy has been considered a very attractive option for the development of hypolipidemic and antidiabetic drugs, but also has profound implications on other facets of metabolic syndrome, like diabetic complications, non-alcoholic fatty liver disease (NAFLD), as well as non-metabolic disorders, including neurodegenerative diseases, cancer, and inflammatory diseases. Recently, a PPARα/γ dual agent, saroglitazar, has been approved in India for NASH treatment. The drug had previously been approved and marketed in India for the treatment of diabetic dyslipidemia and hypertriglyceridemia with type 2 diabetes not controlled by statin therapy [16,17]. Lobeglitazone represents another successful example of the design of dual PPARα/γ agonists; its pharmacological profile together with the absence of severe adverse effects led to its approval by Korean authorities in 2013 for use in patients with T2DM [18,19].

The design and development of triple PPARα/γ/δ agonists aims at the incorporation of the beneficial effects that each receptor has on glucose and lipid metabolism, as well as the elimination of side effects of full PPARγ agonists. Chiglitazar, which is a representative example of this category, was characterized by the American Union of Diabetes as a safe treatment for T2DM in 2019 and was later approved by China's authorities in 2021 as a new effective treatment for TD2M patients [20].

Lanifibranor is one more remarkable triple PPARα/γ/δ agonist, which is a moderately potent and well balanced PPAR pan-agonist with an excellent safety profile. It caused a significant decrease of blood glucose and triglycerides levels in an animal TD2M model; in addition, it decreased liver steatosis, hepatocyte ballooning, and fibrosis in different mouse models of NASH [21,22]. Lanifibranor currently is being tested in a phase III clinical trial.

In our previous studies, we identified the novel naphthalenic derivative AL29-26 (Fig. 1), which showed a very attractive PPAR pan-agonist activity profile: potent full agonist on PPARα and partial agonist on PPARγ and δ subtypes. To gain more insights into the molecular mechanism of PPAR partial or full activation, we solved the crystal structures of AL29-26 bound to PPARα and PPARγ, respectively. In PPARα this ligand occupies a new pocket, similar to the so-called diphenyl pocket of PPARγ, whose filling is allowed by the ligand-induced switching of the F273 side chain from a closed to an open conformation. We demonstrated that the ligand AL29-26 could yet occupy the diphenyl pocket in PPARγ, despite its narrower shape with respect to that of PPARα, but in this position one of its methyls, would make a strong steric clash with the OH of S289, preventing its H-bonding with the carboxylate group and perturbing in this way the efficient H-bond network of the ligand. For this reason, AL29-26 in PPARγ prefers to occupy the typical region of partial agonists, facing the β -sheet and not interacting with H12, and assuming in this way a character of partial agonist (Fig. 1) [23].

The crucial role of the *gem*-dimethyl group of AL29-26 in determining the difference of ligand activity toward PPARα and PPARγ subtypes prompted us to focus our attention on this moiety. Therefore, in a continuous attempt to optimize the pharmacological profile of our compounds, we brought about a series of chemical modifications, which led to the synthesis of compounds **1**—**7** reported in Table 1. Given that PPAR activity is strongly affected by the presence of a stereogenic center close to the carboxylic function of α-aryloxy-alkanoic acids, most of these compounds were prepared as enantiomers. The evaluation of their activity on the three different PPAR subtypes revealed a strong reduction or even a complete loss of activity towards PPARδ; however, we identified some new potent and selective PPARα agonists as well as new ligands showing an interesting PPARα/γ dual activity. Compound (*S*)-**7** turned out to be the ligand with the most interesting pharmacological profile able to potently activate as partial agonist both PPARα and -γ subtypes. In order to gain insights into the possible binding mode of (*S*)-**7** within the PPARα/γ LBD, an X-ray crystallographic analysis was performed. Unexpectedly, in both complexes this partial agonist occupied the same region of the two receptors, filling the hydrophobic pocket typical of full agonists. With the aim to explain this behavior, in vitro experiments as well as docking studies in the presence of PPAR antagonists were performed demonstrating the complexity of the relationship between the binding mode "captured" by the crystal structure and biological activity. In fact, X-ray crystal structure corresponds only to a static representation of the possible interactions between receptor and ligand, whereas the biological activity is the result of a dynamic mechanism, which can involve the whole receptor pocket.

At this point, we decided to evaluate the effects of this compound on steatosis induced by oleic acid overload in human HepG2 cell line. The results showed that (*S*)-**7** strongly counteracted lipid accumulation induced by oleic acid at concentrations much lower than the reference compounds suggesting that it could represent a promising molecule to prevent hepatic steatosis. In addition, we observed that acute treatment of C2C12 muscle cells with micromolar concentration of (*S*)-**7** resulted in a strong enhancement of the glucose uptake. Based upon this latter result, with the aim to examine in depth the mechanism of action of (*S*)-**7**, we decided to verify if these effects could be explained only by transcriptional events following PPAR activation or other mechanisms occurred. We found out that a slight but significant inhibition of the mitochondrial pyruvate carrier could be responsible, at least in part, for the increased glucose uptake we observed in the C2C12 muscle cell line. These results confirmed that (*S*)-**7** also acted through insulin-independent mechanisms, which need other experiments to be elucidated. At this point, with the aim to assess the pharmacological potential of (*S*)-**7**, we decided to evaluate its effects in a streptozotocin (STZ)-

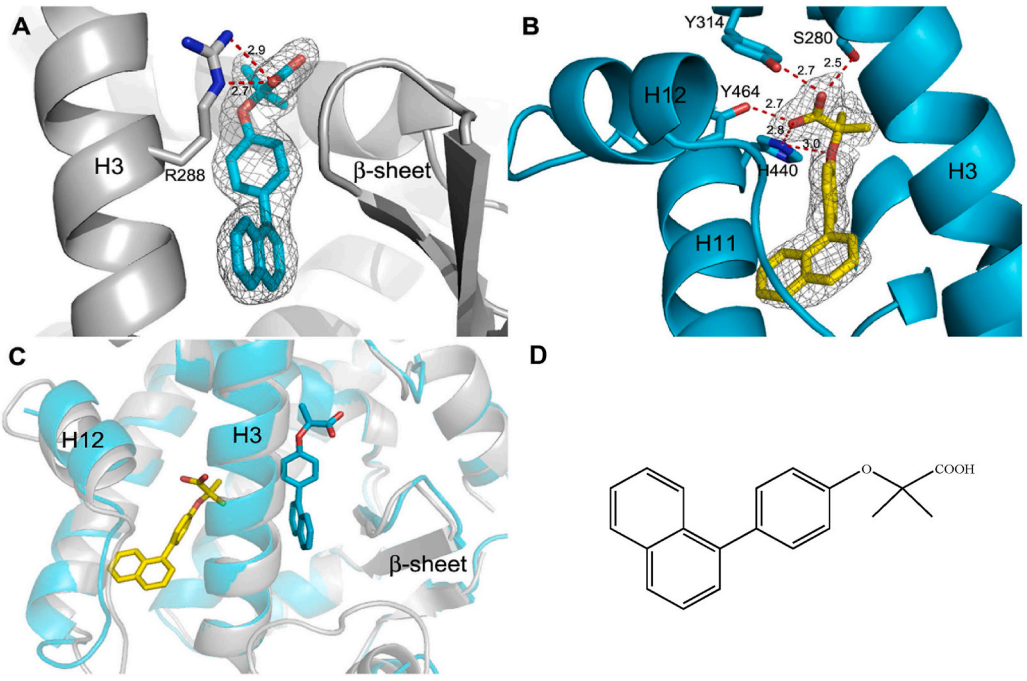

Fig. 1. Binding of AL29-26 to PPARα and PPARγ. (A) Binding mode of AL29-26 (cyan) in the LBD of PPARγ (grey). (B) Binding mode of AL29-26 (yellow) in the LBD of PPARα (cyan); 2Fo-Fc omit maps are shown in mesh and contoured at 1σ. (C) Superposition of PPARα/AL29-26 (ligand yellow, protein cyan) and PPARγ/AL29-26 (ligand cyan, protein grey) crystal structures. (D) Structure of AL29-26.

induced diabetic mouse model. Interestingly, this compound showed a significant reduction in blood glucose and lipid levels displaying, at the same time, no toxic effects on bone, kidney, and liver.

Overall, these results allow to claim that (*S*)-**7**, which combines high potency on PPARα/γ but less efficacy and potentially reduced adverse effects, may represent a very promising candidate as the lead of a new class of drugs for treatment of dyslipidemic type 2 diabetes.

2. Chemistry

AL29–26 and **(*R,S*)-3** were prepared starting from the condensation of 4-bromophenol and acetone or 2-butanone in the presence of bromoform and KOH. The so obtained acids **8** and **9** were converted to the corresponding ethyl and methyl esters, respectively, which were reacted with naphthylboronic acid under Suzuki conditions to give **10** and **11** whose hydrolysis afforded the desired compounds (Scheme 1).

For the synthesis of enantiomers **(*R*)-3** and **(*S*)-3**, the racemic acid **9** was condensed with (*R*)-pantolactone in the presence of DMAP and EDCl to give the diastereomeric esters **(+)-12** and **(−)-12**, which were resolved by fractional crystallization from *n*-hexane. Their reaction with naphthylboronic acid under Suzuki conditions gave the corresponding esters **13** whose hydrolysis allowed to obtain the target enantiomers (Scheme 2).

The absolute configuration of **(*R*)-3** and **(*S*)-3** was determined by chemical correlation. For this purpose, the diastereomeric pantolactone ester **(+)-12** was hydrolyzed affording the *dextro*-enantiomer of acid **9** whose configuration is known to be R [24]. This correlation allowed to assign the R,R configuration to **(+)-12** and consequently to the corresponding final acid **(*R*)-3** (Scheme 3).

1, (*R,S*)-4, **(*R,S*)-5 and (*R,S*)-6** were prepared starting from the condensation of 4-bromophenol and bromo-esters **14a-d** in the presence of NaH in anhydrous DMF (Scheme 4). Compounds **14a-c** were commercially available, whereas **14d** was obtained by treatment of ethyl 2-phenyl-propanoate with N-bromosuccinimmide and 47 % HBr in CCl_4. The so obtained intermediates **15a-d** were reacted with naphthylboronic acid under Suzuki conditions to give **16a-d** whose hydrolysis gave the target compounds.

The synthesis of the enantiomers of compounds **2**, **4**, **5**, and **7** is reported in Scheme 5. 4-Bromophenol was condensed with the optically active 2-hydroxy-esters **17a-d** under Mitsunobu conditions to give the intermediates **18a-d** with inversion of configuration. The enantiomers of **17a** and **17d** were commercially available, whereas **17b** and **17c** were prepared from the optically pure parent amino acids [25] and subsequent esterification with methanol or ethanol. Bromo-esters **18a-d** were then reacted with naphthylboronic acid under Suzuki conditions affording compounds **19a-d** whose hydrolysis gave the target enantiomers.

The enantiomeric excess (ee) of all the final optically active isomers was determined by HPLC analysis on chiral stationary phase (see the Experimental Section).

3. Results and discussion

PPAR Activity. Compounds **1**−**7** were evaluated in vitro for their agonist activity towards the human PPARα (hPPARα), PPARγ (hPPARγ) and PPARδ (hPPARδ) subtypes by employing the GAL4-PPAR transactivation assay. For this purpose, GAL4-PPAR chimeric receptors were expressed in transiently transfected HepG2 cells according to a previously reported procedure [26]. In particular, the results obtained were compared with corresponding data for Wy-14,643, rosiglitazone and L-165,041 used as reference compounds in the PPARα, PPARγ and PPARδ transactivation assays, respectively. Maximum obtained fold induction with the reference agonist was defined as 100 %. The activity of **1**−**7** was also compared with the lead compound AL29-26 (Table 1).

The first chemical modification consisted in the removal of the *gem*-dimethyl group, which led to a compound (**1**) completely inactive on all receptor subtypes. When only a methyl was removed, the corresponding enantiomers (*R*)-**2** and (*S*)-**2** showed similar behaviour compared to AL29-26: full agonists towards PPARα, even though with reduced potency, whereas they displayed lower activity towards PPARγ and PPARδ. The substitution of one methyl group with an ethyl provided compound **3** whose racemic form was about 8 and 1.5 times more potent than AL29-26 on PPARα and PPARγ, respectively; on the contrary, it was poorly effective on PPARδ. Interestingly, the corresponding enantiomers

Table 1
Structure and biological activity of novel analogs of AL29-26 on PPARs.

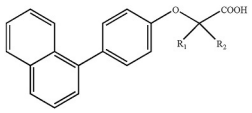

Cpd	R_1	R_2	PPARα EC_{50} μM (E_{max}%)[a]	PPARγ EC_{50} μM (E_{max}%)[a]	PPARδ EC_{50} μM (E_{max}%)[a]
AL29–26	CH_3	CH_3	0.45 ± 0.05 (88 ± 9)	6.3 ± 0.6 (30 ± 2)	13.8 ± 0.9 (64 ± 11)
1	H	H	I	I	i
(*R*)-2	CH_3	H	2.3 ± 1.0 (81 ± 2)	9.3 ± 0.8 (25 ± 1)	(17 ± 7)[b]
(*S*)-2	CH_3	H	1.8 ± 0.4 (112 ± 3)	13.9 ± 1.2 (22 ± 1)	(12 ± 1)[b]
(*R,S*)-3	CH_3	Et	0.062 ± 0.008 (95 ± 10)	4.52 ± 0.24 (25 ± 1)	(17 ± 3)[b]
(*R*)-3	CH_3	Et	0.311 ± 0.045 (50 ± 1)	4.3 ± 0.6 (19 ± 2)	(17 ± 2)[b]
(*S*)-3	CH_3	Et	0.030 ± 0.005 (83 ± 2)	4.7 ± 0.6 (15 ± 1)	(12 ± 1)[b]
(*R,S*)-4	Et	H	0.46 ± 0.08 (94 ± 10)	10.00 ± 0.22 (35 ± 2)	i
(*R*)-4	Et	H	1.42 ± 0.32 (61 ± 8)	7.3 ± 0.5 (31 ± 2)	i
(*S*)-4	Et	H	0.183 ± 0.029 (84 ± 10)	11.0 ± 0.5 (33 ± 3)	i
(*R,S*)-5	i-Pr	H	0.66 ± 0.31 (85 ± 11)	11.6 ± 1.5 (10 ± 2)	i
(*S*)-5	i-Pr	H	0.16 ± 0.04 (85 ± 7)	11.5 ± 2.8 (24 ± 9)	i
(*R,S*)-6	Ph	CH_3	0.060 ± 0.024 (63 ± 2)	4.3 ± 2.2 (17 ± 3)	i
(*R*)-7	Bz	H	i	I	i
(*S*)-7	Bz	H	0.061 ± 0.005 (58 ± 3)	1.42 ± 0.36 (27 ± 2)	i
Wy-14,643			1.56 ± 0.30 (100 ± 10)	–	–
rosiglitazone			–	0.039 ± 0.003 (100 ± 9)	–
L-165,041			–	–	1.6 ± 0.3 (100 ± 10)

[a] Efficacy values were calculated as a percentage of the maximum obtained fold induction with the reference compounds; i = inactive at concentration up to 25 μM; b = efficacy values at 50 μM (lower doses were inactive, higher doses were toxic).

showed similar activity on PPARγ and PPARδ, whereas the S-isomer was a PPARα full agonist 10-fold more potent than the R-isomer. In compound **4** one methyl group of AL29-26 was removed, the other one was substituted by an ethyl: the racemate did not show any significative difference towards PPARα and PPARγ, whereas it was inactive on PPARδ. However, also in this case PPARα exhibited a pronounced stereoselectivity being (*S*)-**4** about 8 times more potent than (*R*)-**4**. The same behaviour was obtained by introduction of the branched *i*-propyl group in place of the ethyl leading to compound **5**; in this case, it was prepared only the S-isomer, which, still, showed to be 4-fold more active than racemate only towards PPARα. In compound **6**, one of the methyl groups of AL29-26 was replaced by a phenyl obtaining a potent, even though less effective, PPARα agonist with an EC_{50} 8-fold lower than that of AL29-26; in addition, this compound proved to be poorly active on PPARγ and inactive on PPARδ shaping up to be therefore a good selective PPARα ligand. We tried to prepare both enantiomers of **6**, but all attempts made so far resulted unsuccessful. Finally, we synthesized both stereoisomers of compound **7** with a benzyl group alpha to the carboxylic function; in this case, (*R*)-**7** resulted completely inactive towards all of three subtypes, whereas the activity resided only in the S-isomer, which turned out to be a dual PPARα/γ partial agonist with a higher potency than AL29-26 on both subtypes. Given its interesting pharmacological profile and synthetic feasibility, we decided to focus our attention on this compound for further evaluation.

Binding of (S)-7 to PPARα and PPARγ. In order to gain insights into the possible binding mode of the ligand (*S*)-**7** within the PPARα/γ LBD, the crystal structures of the two subtypes were solved collecting diffraction data from apo-crystals soaked for a few days with the ligand at 0.5 mM. As evidenced by the superposition in Fig. 2, in both complexes the ligand occupied the same region of the two receptors, filling the hydrophobic pocket between helices 3, 11 and 12.

As regards the complex PPARα LBD/(*S*)-**7**, the crystal structure showed that the polar head of (*S*)-**7** was engaged in a very efficient network of H-bonds with the side chain of Y464 (2.52 Å) belonging to helix 12, Y314 (2.75 Å), H440 (2.72 Å) and with the OH group of S280 (2.52 Å). Even in this case, as already reported for the ligand AL29-26 (PDB ID 5HYK) [23], the ligand binding within the hydrophobic pocket was only possible thanks to the displacement of the side chain of F273, which made an additional portion of the cavity accessible for bulky ligands. Interestingly, although having the same scaffold of AL29-26 and occupying the same region of the receptor, (*S*)-**7** acted only as a partial agonist (E_{max} 58 % vs 88 % of AL29-26). A possible explanation could lie in the ability of (*S*)-**7** to induce a slightly different conformation of the loop connecting helices 11 and 12 with respect to the PPARα LBD/AL29-26 complex. In fact, a visual inspection revealed that in the case of PPARα LBD/AL29-26 complex, the loop was closer to H3; the distance between residues A454 (CB) and V270 (CG1), taken as reference residues, increases from 3.4 to 4.1 Å, respectively. Therefore, (*S*)-**7** might induce a less effective stabilization of H12, which, in turn, might result in differences in co-activators recruitment and binding.

Within the PPARγ LBD, the ligand interacted directly with the residues of the canonical triad (Y473, H323 and H449). The rigid and bulky aromatic groups of the ligand occupied a region of the hydrophobic pocket, the so-called diphenyl pocket, usually filled by the aromatic ring of F282, which switched from the generally adopted extended to a gauche (+) conformation, thus allowing the ligand accommodation. A comparable side chain flipping mechanism was already described in our previous works with the ligands LT175 (PDB ID 3B3K) [27] and LJ570 (PDB ID 6F2L) [28], sharing a similar molecular scaffold and binding profile with (*S*)-**7** (Figure S1 of the SI). Actually, LJ570 was found to also adopt another position in the PPARγ LBD obtained from a different soaking time and ligand concentration (Fig. 3); in this case, LJ570

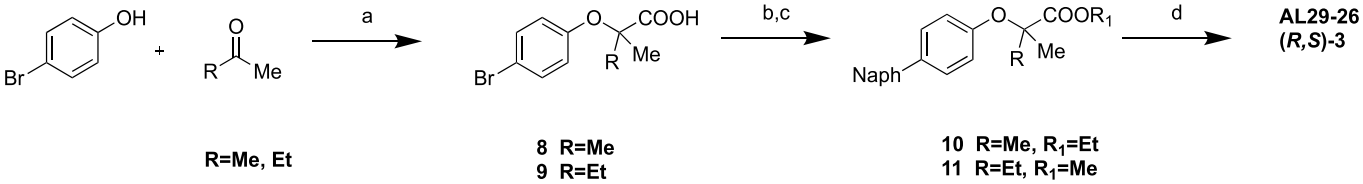

Scheme 1. (a) KOH, $CHBr_3$, r.t. overnight; (b) EtOH or MeOH, H_2SO_4, reflux 2–4 h; (c) naphthalene-1-boronic acid, Cs_2CO_3, $Pd(PPh_3)_4$, dry toluene, reflux 5 h; (d) 2 N NaOH, THF, r.t. 4 h.

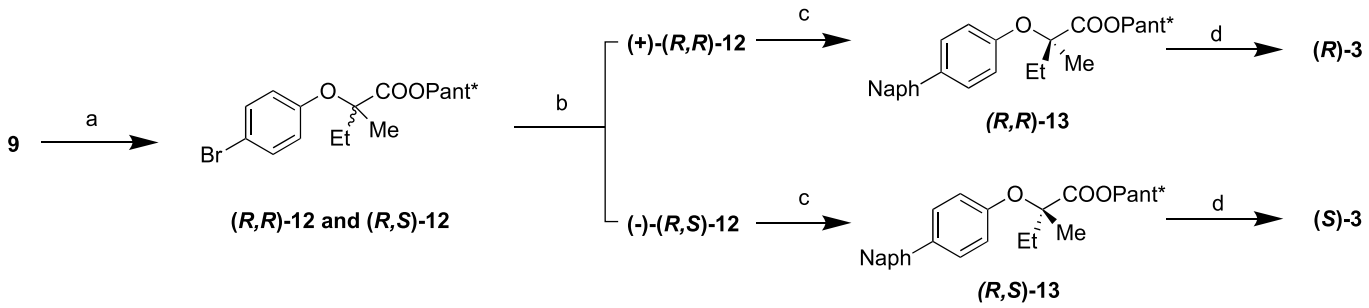

Scheme 2. (a) (*R*)-pantolactone, DMAP, EDCI, CH_2Cl_2, r.t. 24 h; (b) fractional crystallization from *n*-hexane; (c) naphthalene-1-boronic acid, Cs_2CO_3, $Pd(PPh_3)_4$, dry toluene, reflux 5 h; (d) 2.5 N NaOH, 2-propanol, reflux overnight.

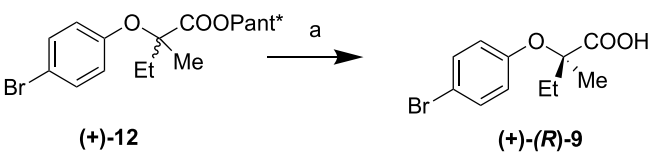

Scheme 3. (a) 2.5 N NaOH, 2-propanol, 65 °C overnight.

accommodated between H3 and the β-sheet, which is the typical position of the partial agonists, allowing to hypothesize the existence of an equilibrium between two different binding modes [28].

With the aim to verify the possibility that (*S*)-**7** is able to occupy a different pocket when the canonical site is blocked, we performed a cotransfection assay by preincubating cells with **20** (GW9662, Fig. 4, upper part) before treatment with (*S*)-**7**. **20** is a commercially available PPARγ antagonist that binds to the canonical site of PPARγ through a covalent thioether bond with C285 [29]. It was previously shown that **20** blocks the binding of many PPARγ ligands to the canonical site, whereas no effect has been reported on the site of partial agonists [28,30,31]. In our experiment, as shown in Fig. 4B, the presence of **20** did not affect the activity of *(S)*-**7**, but even slightly increase its potency allowing to suppose its binding to the site of partial agonists with affinity similar to that for the canonical site. On the contrary, **20** blocked the action of pioglitazone at concentrations up to 25 μM (Fig. 4A). With the aim to confirm the binding of *(S)*-**7** to this site, we performed the cotransfection assay by preincubating cells with **21** (SR16832, Fig. 4, upper part), which is a PPARγ covalent antagonist derived from the enlargement of the 2-chloro-5-nitrobenzamidyl scaffold of **20**. This modification allows **21** to accommodate into the canonical site and protruding into the partial agonist binding site simultaneously blocking, therefore, both ligand binding modes [32]. In this experiment, as shown in Fig. 4A and B, the presence of **21** blocked the action of both pioglitazone and *(S)*-**7** at concentrations up to 25 μM. As a whole, it seems reasonable to assert that the partial agonist activity of *(S)*-**7** derives from the existence of an equilibrium between two different positions into the PPARγ binding pocket.

To investigate the binding mode of (*S*)-**7** into the **20**-bound PPARγ LBD, a molecular docking simulation was performed using Glide (Glide, Schrödinger, LLC, New York, NY, 2021) [33]. PPARs are characterized by a "Y shaped" ligand binding domain (LBD), which is composed of a polar arm I, extending toward H12 (a crucial part of the activation function AF-2), a hydrophobic arm II, which is surrounded by H3 and the β-sheet, and a hydrophobic entrance (arm III). Arm II partly overlaps with a region of the LBD often referred to as "alternate site", a rather solvent exposed area lined by the functionally important and flexible Ω-loop [28,30,32,34–38]. The ability of agonist ligands to bind within arm I and more strongly stabilize the AF-2 surface has been connected to increased transcriptional activation, whereas partial agonism has been

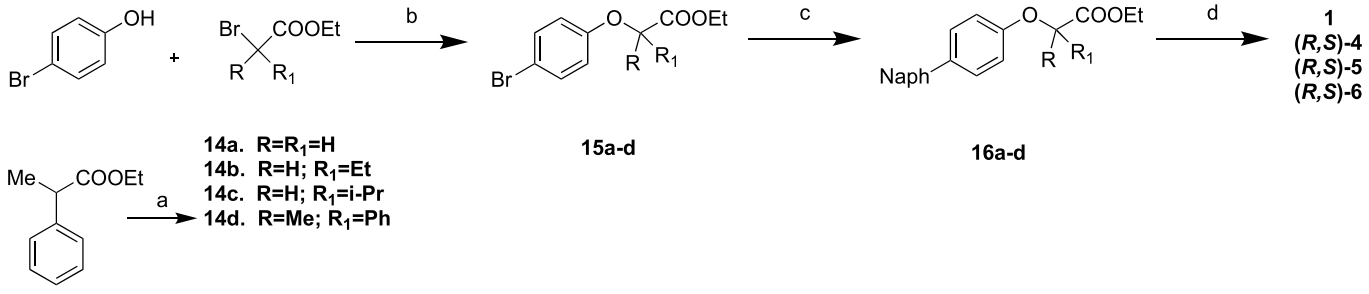

Scheme 4. (a) NBS, 47 % HBr, AcOH, CCl_4, reflux 24 h; (b) NaH, dry DMF, reflux 6 h; (c) naphthalene-1-boronic acid, Cs_2CO_3, $Pd(PPh_3)_4$, dry toluene, reflux 5 h; (d) 2 N NaOH, THF, r.t. 4 h.

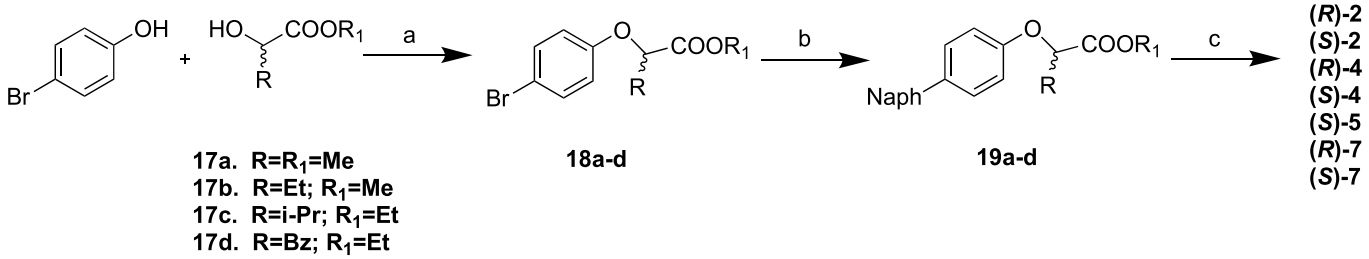

Scheme 5. (a) PPh_3, DIAD, dry THF, r.t. overnight; (b) naphthalene-1-boronic acid, Cs_2CO_3, $Pd(PPh_3)_4$, dry toluene, reflux 5 h; (c) 2 N NaOH, THF, r.t. 4 h.

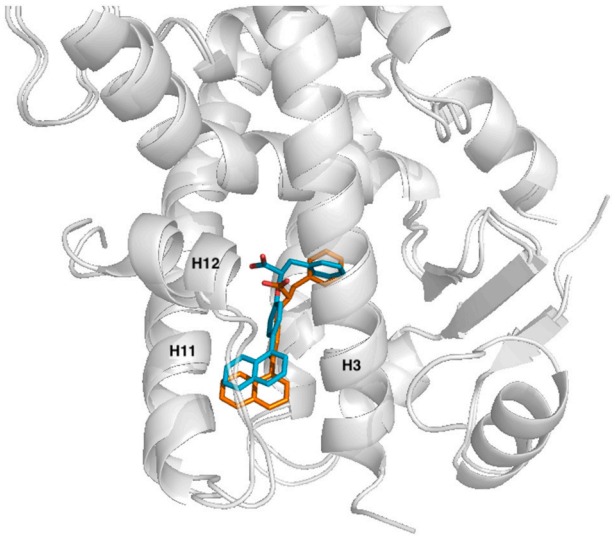

Fig. 2. Superposition of (*S*)-**7** within PPARγ-LBD (cyan) and PPARα-LBD (orange).

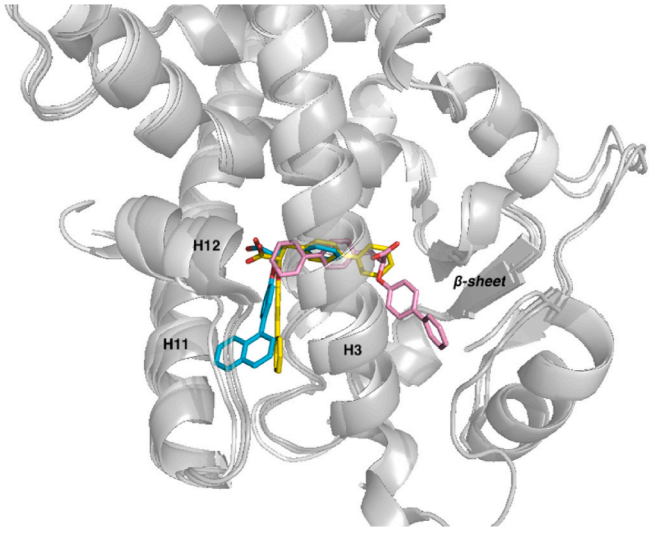

Fig. 3. Superposition of PPARγ-LBD/(*S*)-**7** complex with two different PPARγ-LBD/LJ570 complexes, obtained with short-time soaking at low concentration (pink, PDB ID 4JL4) and long-time soaking at high concentration (yellow, PDB ID 6F2L).

associated to ligands that bind to arm II or do not interact with H12 and arm I [39]. It was previously reported that co-binding of a synthetic ligand to the canonical pocket can push endogenous PPARγ ligands towards the alternate site. Binding to this alternate site could synergistically affect the structure and function of the receptor and influence coactivator recruitment [34].

From the results of the docking simulation, (*S*)-**7** in the presence of the antagonist **20** is predicted to occupy arm II, towards the alternate site (Fig. 5A), with both compounds simultaneously accommodated into the PPARγ LBD. In detail, (*S*)-**7** accepted an H-bond from the main chain nitrogen of S342 on the β-sheet; moreover, the ligand's bulky and hydrophobic scaffold engaged additional interactions with residues I341, F264 and L255 on H2′, R280 on H3. The benzyl group of (*S*)-**7** interacted also with the terminal phenyl group of **20**, which is covalently bound to C285 on H3. In order to probe the stability of the interactions predicted by docking and to take into account the effects of the solvent in mediating the ligand/protein contacts, the obtained ternary complex PPARγ/**20**/(*S*)-**7** was then subjected to 100 ns molecular dynamics (MD) with Desmond [40]. The results suggested that both compounds were well stabilized within the receptor LBD, with very slight rearrangements to achieve a better fit (Fig. 5B). The RMSD analysis of both protein and ligand revealed stable trajectories (Figure S2 of the SI). (*S*)-**7** formed a network of water-bridged hydrogen bonds linking the carboxylate group of the ligand with E343 and L340 on the β-sheet. The interaction with S342 was very stable through the entire simulation and was also further stabilized by water, as shown in Fig. 5B and S3 of the SI. The overlay of the structural complex obtained after the 100 ns MD on the dual-site antagonist **21** (Figure S4 of the SI) revealed that this bulkier ligand clashes with (*S*)-**7** because of the presence of the 6-methoxyquinoline ring, thus explaining the loss of activity observed in cotrasfection assays. As a result, (*S*)-**7** remains active in the presence of the smaller antagonist **20**, also due to its ability to relocate within the arm II/alternate site. In fact, we could observe a certain overlap of (*S*)-**7** with ligands co-crystallized within the alternate site, namely T2384 (PDB 3K8S) [36] and S35 (PDB 5GTO) [37] (Figure S5 of the SI).

The partial agonism exerted by (*S*)-**7** on PPARα was further confirmed when we performed a cotransfection assay by preincubating cells with **20** before treating cells with our ligand. Indeed, in PPARα **20** is able to act as both an antagonist, reducing the activation induced by full agonists, and as an agonist, enhancing the activation induced by less effective agonists, such as fibrates [41]. In fact, in our experiment, as shown in Fig. 6, the presence of **20** produced a clear additive effect with *(S)*-**7**, whereas, on the contrary, reduced the efficacy of Wy-14,643.

To investigate the binding mode of (*S*)-**7** into the **20**-bound PPARα LBD, we carried out a similar in silico analysis as detailed above for PPARγ. Interestingly, the X-ray structures of PPARα with **20** and fibrates revealed that three molecules of **20** were covalently linked to C275, C278 and C276, thus occupying most of the arm II pocket [41]. Therefore, we employed the structure of PPARα LBD in complex with **20** and fenofibric acid (PDB 6L36). Docking of (*S*)-**7** into the structure of PPARα revealed that, in this case, the ligand occupied arm I, forming the well-recognized network of H-bonds with Y464, Y314, H440 and S280 through the carboxylate moiety. During the MD simulation (*S*)-**7** mostly maintained such interactions, in particular the H-bond with Y464 on H12 (Fig. 7A–B and S7 of the SI), whereas the H-bond with H440 was less stable; a new one was instead established with Q277. Main ligand movements involved a slight repositioning of the naphthyl group within the hydrophobic pocket. On comparing the docked pose and the conformation obtained at the end of the MD simulation of (*S*)-**7**, we could observe a nice overlap with the fenofibric acid co-crystallized in the presence of the three molecules of **20** (Figure S8 of the SI). Therefore, we could hypothesize that in PPARα **20** enhances the receptor activation induced by (*S*)-**7**, as observed previously for fibrates [41]. On the other hand, **20** was found to reduce the activity of the reference full agonist Wy-14,643 in cotrasfection assays. In order to rationalize these outcomes, we resorted to the same in silico analysis by performing docking of Wy-14,643 into PPARα LBD in complex with **20**, followed by MD simulations. The presence of **20** caused Wy-14,643 to substantially rearrange within arm I (Fig. 7C–D and S11 of the SI), with respect to the experimentally determined binding mode (PDB 6KBA), likely to avoid steric clashes; however, during the course of the simulation, the H-bond with Y464 became less stable and was definitely lost in the final frames (Figure S10 of the SI). Thus, the loss of activity of Wy-14,643 observed in the presence of **20** might be ascribed to a less effective stabilization of H12.

Effects of (S)-7 on steatosis. To further characterize the pharmacological profile of (*S*)-**7**, we decided to evaluate its activity on steatosis induced by oleic acid overload in human HepG2 cell line. The results were compared with those obtained from fenofibrate and rosiglitazone which were used as reference ligands. Steatosis was induced in HepG2 cells by oleic acid overload for 24 h. The effects of (*S*)-**7** were evaluated after incubation for further 72 h with a growth medium containing oleic acid and the ligands. As depicted in Fig. 8, all tested ligands strongly

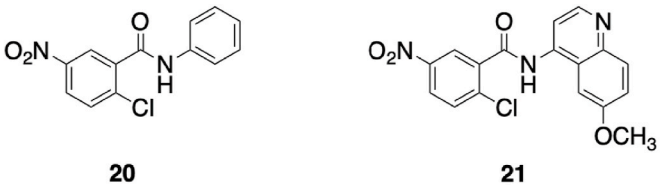

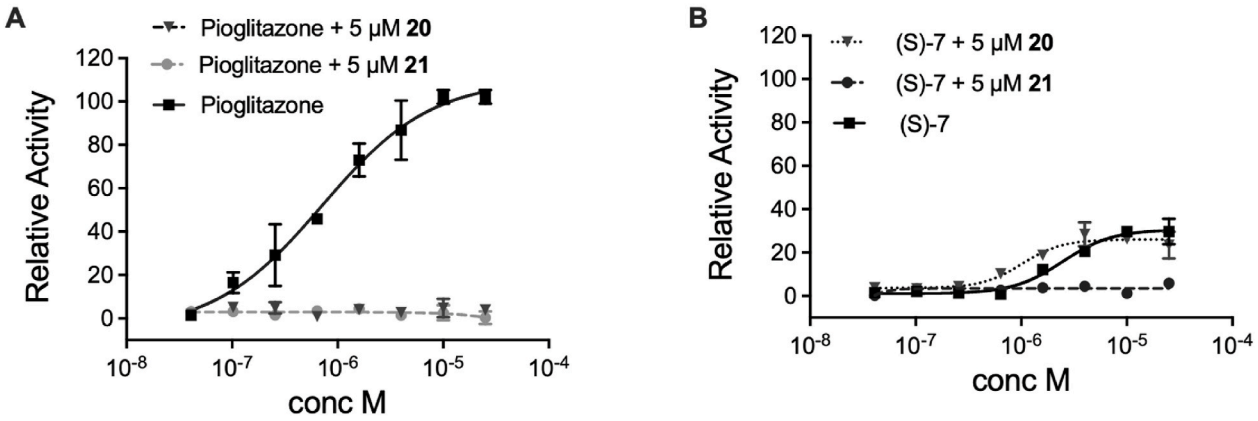

Fig. 4. Luciferase reporter assay showing the concentration-dependent effects on PPARγ transactivation of (A) pioglitazone and (B) (*S*)-**7** in the presence or not of PPARγ covalent antagonists **20** and **21**.

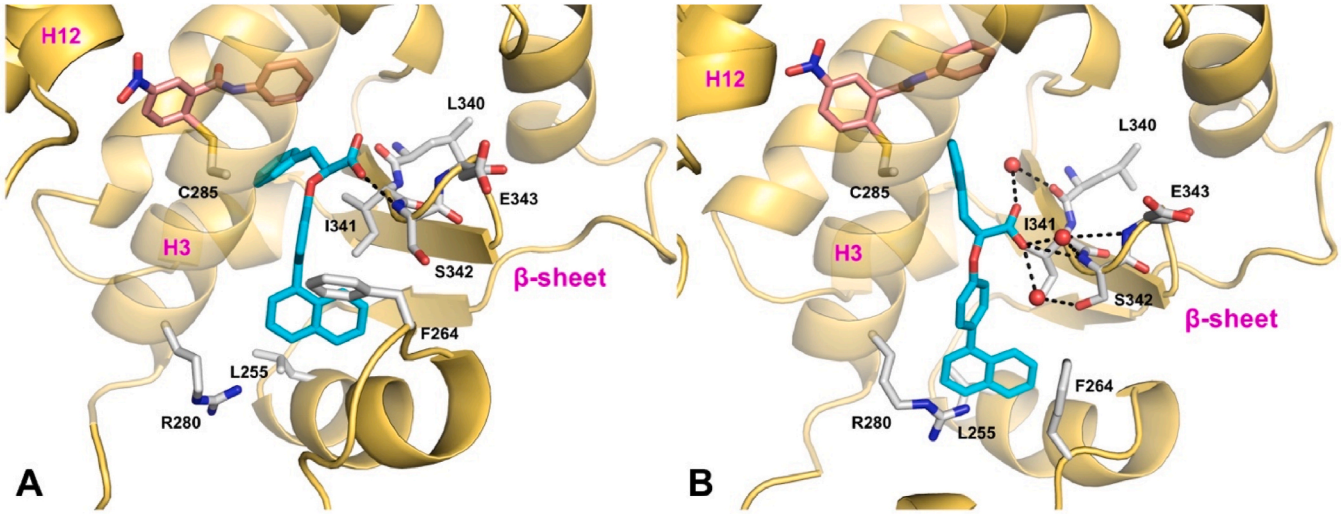

Fig. 5. Binding mode of (*S*)-**7** (cyan sticks) into the **20**-bound PPARγ LBD (represented as a yellow ribbon model) as predicted by (A) docking and (B) at the end of 100 ns MD simulation. The covalently bound **20** is shown as salmon sticks. Only amino acids discussed in the main text are displayed (white sticks) and labeled. H-bonds discussed in the text are depicted as dashed black lines. Water molecules are depicted as red spheres.

counteracted lipid accumulation induced by oleic acid; however, (*S*)-**7** produced this effect at concentrations 100 and 2500 times lower than rosiglitazone and fenofibrate, respectively. These results suggest that (*S*)-**7** is a promising compound to prevent hepatic steatosis.

Experimental design. Liver cells were treated with oleic acid (OA) 1 mM for 24 h to induce steatosis and then treated with the indicated ligand or vehicle, in the presence of oleic acid, for additional 72 h. After this time, intracellular lipid content was determined by staining cellular lipids with 0.5 % Oil Red O. The quantification of the intracellular dye was performed after isopropanol extraction and spectrophotometric reading at 490 nm with a Biorad 550 microplate reader. All tests were carried out in quadruplicate. Data obtained were normalized respect to protein content and reported as percent of the control test. Data showed in the figure represent the mean values ± SD. *p < 0.05; **p < 0.01.

Effects of (S)-7 on mitochondrial pyruvate carrier (MPC). TZD drugs act as insulin sensitizers and are agonists of PPARγ, which mediates many of their beneficial effects. However, TZDs are known to interact with additional molecular targets and can affect metabolism by mechanisms other than transcription regulation. In particular, they are able to interact with the mitochondrial pyruvate carrier (MPC) complex, which is a heterodimeric complex that mediates the transport of pyruvate generated by glycolysis across the inner mitochondrial membrane into the mitochondrial matrix. This is an important and rate-limiting step in intermediary metabolism, and its inhibition results in protection from diabetes, liver injury, and other high-fat (HF) diet−induced metabolic derangements [42]. Very recently, also a novel PPARα/γ dual agonist has been shown to produce a slight but significant inhibition of MPC, which has been considered as the effect responsible of a rapid increase in

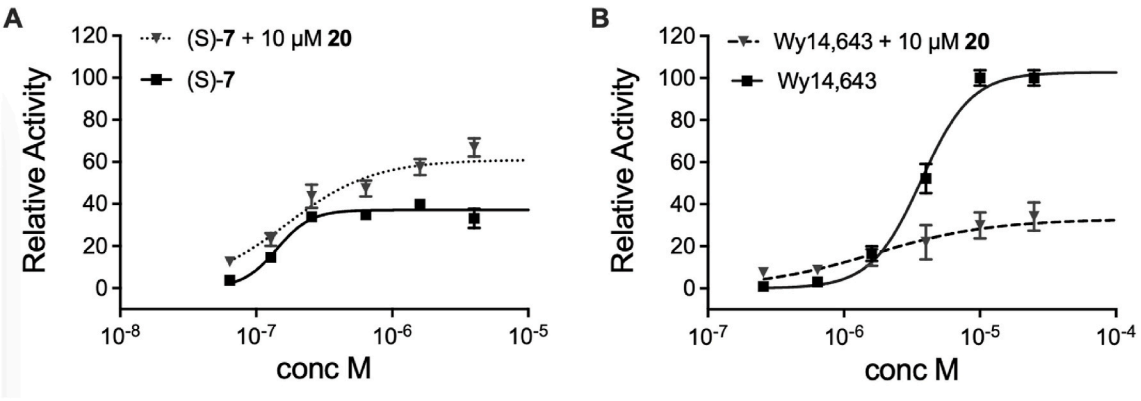

Fig. 6. Luciferase reporter assay showing the concentration-dependent effects on PPARα transactivation of (A) (*S*)-**7** and (B) Wy-14,643 in the presence or not of PPARα covalent ligand **20**.

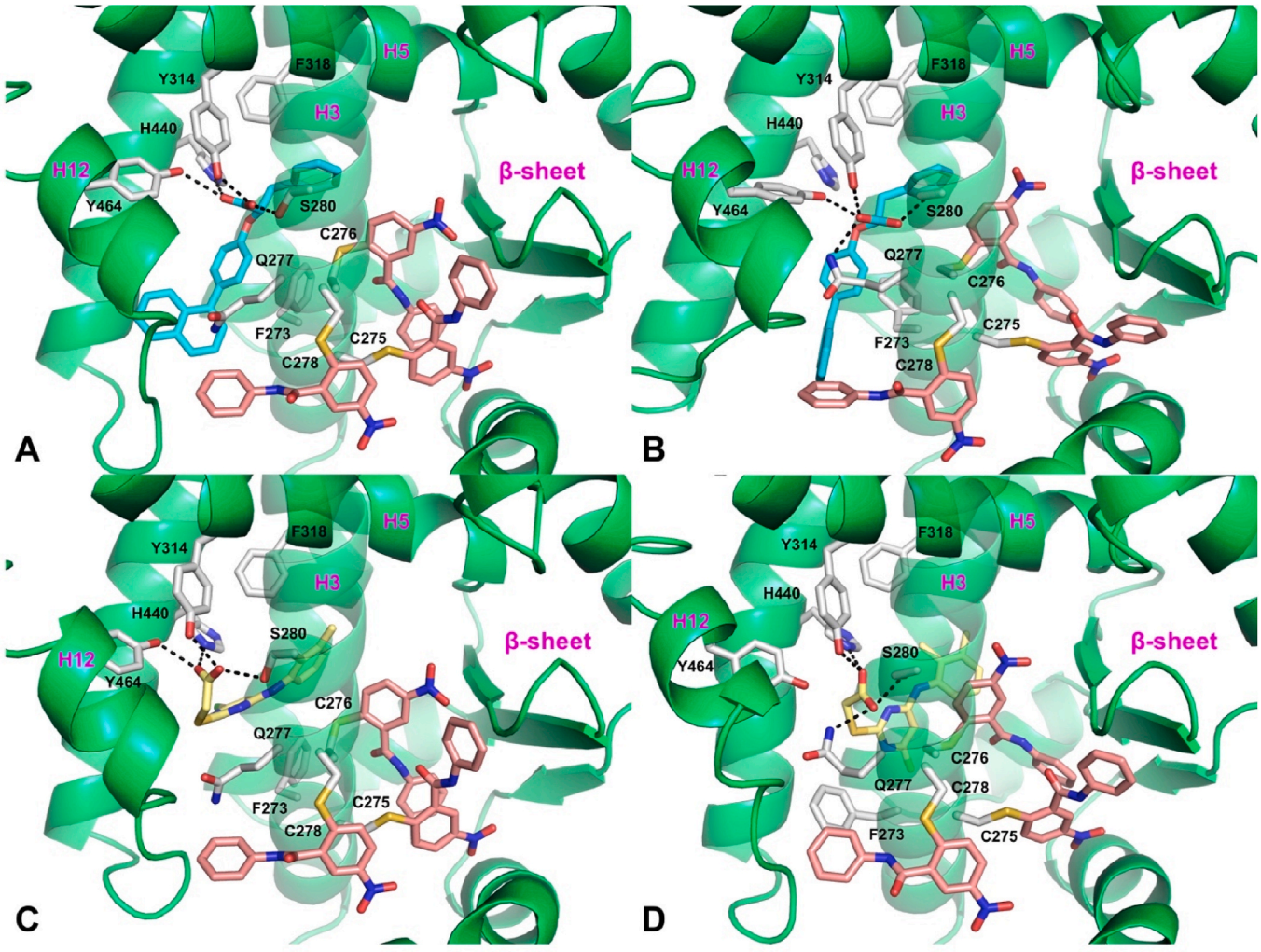

Fig. 7. Binding mode of (*S*)-**7** (cyan sticks) and Wy-14,643 (pale yellow sticks) into the **20**-bound PPARα LBD (represented as a green ribbon model) as predicted by (A–C) docking and (B–D) at the end of 100 ns MD simulation, respectively. The covalently bound **20** is shown as salmon sticks. Only amino acids discussed in the main text are displayed (white sticks) and labeled. H-bonds discussed in the text are depicted as dashed black lines.

glucose uptake from murine myoblasts. This effect was too rapid to be attributable to the ability of this compound to act as a PPAR agonist and, interestingly, did not provoke reduction in basal oxygen consumption and ATP production, which are observed, instead, with rosiglitazone [43]. Therefore, considering the structural similarity of this compound with (*S*)-**7**, we decided to evaluate the effects of our compound on glucose uptake in C2C12 cell line. Fig. 9 confirms that acute treatment of these muscle cells with micromolar concentration of compound (*S*)-**7** resulted in a strong enhancement of the glucose uptake with an insulin-independent mechanism, as demonstrated by evidence that (*S*)-**7**−insulin co-stimulation did not increase glucose uptake compared to treatment with (*S*)-**7** alone. At the same time, in this experiment, we

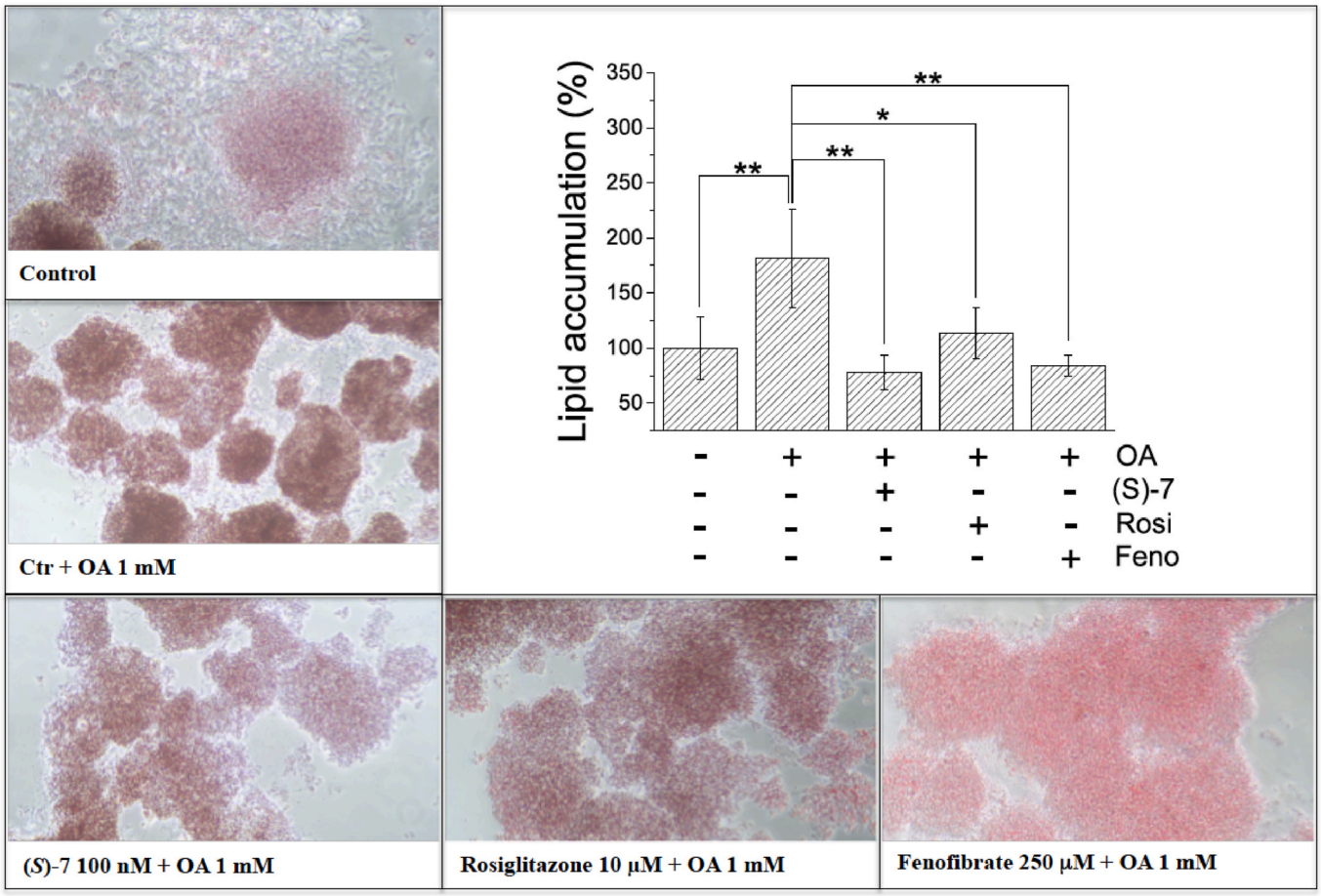

Fig. 8. Biological activity of (*S*)-**7** in hepatic cells.

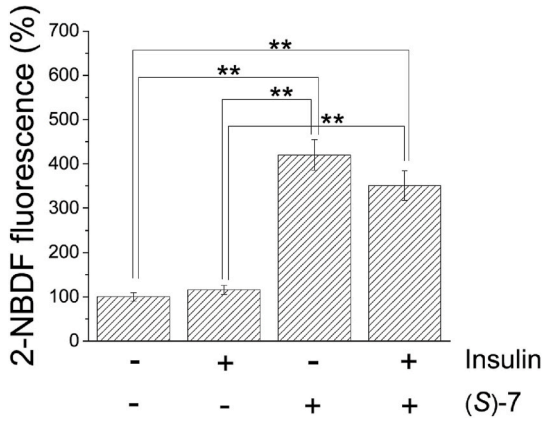

Fig. 9. Glucose uptake assay. C2C12 myoblasts were starved for 24 h and then incubated for 30 min with a starvation medium containing 50 μM (*S*)-**7**, 10 nM insulin, or the combination (*S*)-**7**−insulin. After this time, cells were washed with PBS and incubated with the starvation medium containing 40 μM 2-NBDG for 3 h. Finally, cells were washed, trypsinized, and analyzed using flow cytometry. All tests were carried out in triplicate. Data obtained were normalized with respect to the control sample and reported as the mean ± SD. The differences between series of data were statistically analyzed using the unpaired Student's T test. **$p < 0.01$.

proved that (*S*)-**7** strongly increased glucose uptake after only 30 min. This acute effect suggested that the enhanced glucose transport activity might not be entirely explained by transcriptional events associated with PPAR activation.

At this point, to evaluate the possible inhibition of MPC by (*S*)-**7**, we compared the bioenergetics profile of C2C12 cells with that of C2C12 cells treated with rosiglitazone and (*S*)-**7**. We observed that treatment with rosiglitazone, as expected, impaired oxygen consumption and ATP production inducing, at the same time, acidification of the external growth medium (Fig. 10A–D). This is a consequence of the MPC inhibition resulting in a reduction of pyruvate uptake and its conversion to lactate, which is then extruded in the extracellular milieu. In this way, a general slowdown of cellular metabolism occurs, without however significantly unbalancing the ratio between respiratory and glycolytic capacity of muscle cells. This hypothesis is confirmed by evidence that the OCR/ECAR ratio did not change in C2C12 cells treated with 10 μM rosiglitazone (Fig. 10E). On the other hand, we found that treatment with (*S*)-**7** significantly stimulated the acidification of the external growth medium, without, however, impairing oxygen consumption and ATP production of muscle cells (Fig. 10A–D). This suggests that C2C12 cells treated with (*S*)-**7** increased the uptake and metabolism of glucose to enhance pyruvate production and try to overcome the (*S*)-**7** induced block of MPC. This block enhanced pyruvate conversion to lactate and, at the same time, forced the cells to compensate the reduced entrance of pyruvate into the mitochondria by increasing oxidation of other metabolic substrates such as fatty acids and thus enhancing the OCR/ECAR ratio (Fig. 10E). This mechanism could also explain the results of (*S*)-**7** on steatosis, which showed that chronic stimulation with nanomolar concentrations of (*S*)-**7** strongly reduced lipid deposits into HepG2 cells in a manner more efficient than rosiglitazone and fenofibrate. Taken together, these data confirmed that (*S*)-**7** is able to increase the uptake and metabolism of glucose and enhance mitochondrial activity by boosting fatty acid degradation, thus avoiding lipid accumulation in liver or muscle cells.

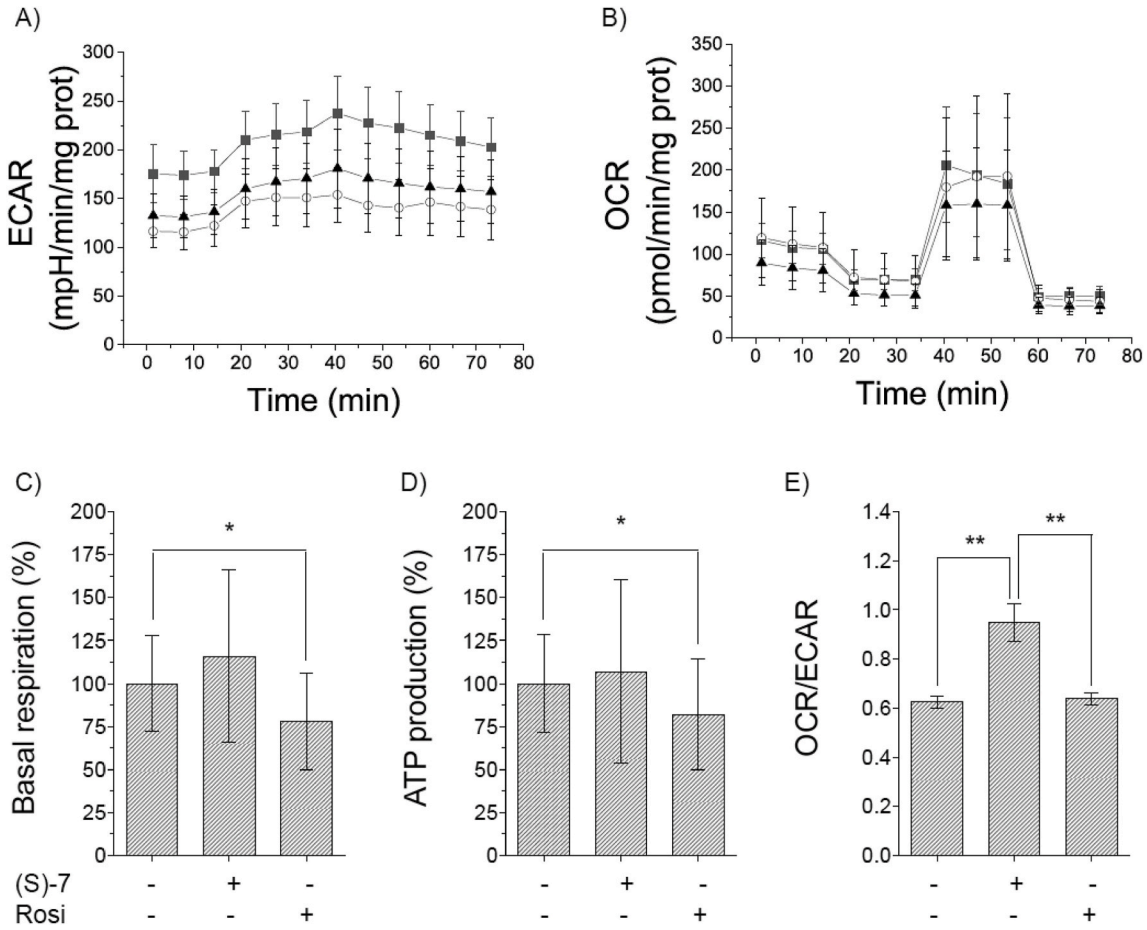

Fig. 10. Mito Stress analysis of C2C12 cells obtained using the Seahorse XF Pro analyzer (Agilent). C2C12 cells were plated and incubated for 24 h in the presence of 100 nM (*S*)-**7** (◯) and 10 μM rosiglitazone (▲) before analysis. The control test (■) was performed by adding an equivalent volume of DMSO, the solvent used to dissolve (*S*)-**7** and rosiglitazone, to the plates. For each test, 8–12 analyses were performed. The data obtained were normalized for protein content. The data reported in the figure represent the mean value ± SD. (A), extracellular acidification rate (ECAR); (B), oxygen consumption rate (OCR); (C, D) basal respiration and ATP production calculated from data reported in figure (B); (E), OCR/ECAR ratio. * indicates p value < 0.05; ** indicates p value < 0.01.

In Vivo Pharmacokinetic Study of Compound (S)-7. A bioavailability study of (*S*)-**7** was carried out in male Sprague−Dawley rats, and the pharmacokinetic parameters are presented in Table 2. Following a single intravenous (IV) administration of (*S*)-**7** formulation at 1 mg/kg, the mean plasma clearance (Cl) was found to be very low, 1.42 mL/min/kg, which is approximately 0.026-fold lower than normal hepatic blood flow of rats. The volume of distribution was found to be 0.581 L/kg, which was approximately 1.2-fold lower than total body fluids in rats (0.7 L/kg), indicating fairly high distribution in tissues. The terminal plasma elimination half-life ($T_{1/2}$) was also found to be fairly high (4.74 h). After a single oral (PO) gavage administration of (*S*)-**7** formulation at 5 mg/kg, the median time to reach the maximum plasma concentration (T_{max}) was found to be 2 h. The exposure was found to be 4280 ng/mL (C_{max}) and 43600 h ng/mL (AUC_{last}). The absolute oral bioavailability was 76.4 %.

In Vivo Antihyperglycemic Screening. An STZ-induced diabetic mouse model was used to evaluate the antihyperglycemic activity of test compound (*S*)-**7** alone or in combination with reference standard pioglitazone. The test dose was fixed based on the predicted LD50 value [44]. Doses lower than 1/50th and 1/100th of the predicted LD_{50} value were used for the study. Diabetic mice were orally treated with the test compound at a dose of 25 mg/kg (group 3) and 50 mg/kg body weight (group 4) for a period of 15 days. The fasting blood glucose level of control (group 6), diabetic-untreated (group 1), and diabetic-treated (groups 2−5) mice was tested on days 0, 5, 10, and 15 of the screening period (Table 3). Data were statistically analyzed by one-way ANOVA followed by Dunnett's *t*-test using R Package.

Table 2
Mean pharmacokinetic parameters following a single intravenous (IV) bolus and oral (PO) administration of (*S*)-7 in male sprague-dawley rats[a].

Parameters	Compound (*S*)-7	
	IV (1 mg/kg)	PO (5 mg/kg)
Dose Volume (mL/kg)	10	10
C_0/C_{max} (ng/mL)	2300 ± 380 (C_0)	4280 ± 190 (C_{max})
T_{max} (h)	0.083	2
AUC_{last} (h·ng/mL)	11400 ± 202	43600 ± 8390
$AUC_{infinity}$ (h·ng/mL)	11800 ± 281	49000 ± 8180
$T_{1/2}$ (h)	4.74 ± 0.375	7.61 ± 2.86
V_d (L/kg)	0.581 ± 0.0352	1.16 ± 0.525
Cl (mL/min/kg)	1.42 ± 0.0343	1.74 ± 0.314
MRT_{last} (h)	6.04 ± 0.394	7.74 ± 0.519
%F	–	76.4 ± 14.7

[a] C_0/C_{max}: maximum plasma concentration; T_{max}: time to reach the maximum plasma concentration; AUC_{last}: area under the curve from time zero to the last measurable concentration; $AUC_{infinity}$: area under the curve from time zero to infinity; $T_{1/2}$: plasma elimination half-life; V_d: volume of distribution; MRT_{last}: Mean Residence Time to the last concentration; Cl: plasma clearance; F: oral bioavailability.

Compared to normoglycemic control (group 6), diabetic control animals (group 1) showed severe hyperglycemia. On day 0, the mean blood glucose level in the diabetic control group was 365 ± 54.25 mg/

dL and increased to a level of 435.2 ± 46.89−456.8 ± 63.77 mg/dL during the period from days 5–15. Treatment with the standard drug pioglitazone (30 mg/kg, group 2) showed a gradual decrease in blood glucose level from days 5–15, which became significant at days 10 and 15 (248 ± 25.97 and 224.2 ± 28.28 mg/dL, respectively) compared to group 1. Treatment with the test compound at the dose of 25 mg/kg (group 3) showed equivalent effects to 30 mg/kg of pioglitazone, whereas a higher reduction of blood glucose level was obtained by a dose of 50 mg/kg (group 4). These results demonstrate that there is a dose-dependent response for (*S*)-**7**. In addition, we decided to evaluate a co-treatment (group 5) with (*S*)-**7** (25 mg/kg) and pioglitazone (30 mg/kg). A clear additive effect was obtained; in fact, group 5 showed basically the same significant decrease in blood glucose level of group 4.

In Vivo Lipid Profiling. Total cholesterol (TC), triglyceride (TG), high-density lipoprotein cholesterol (HDL-C), low-density lipoprotein cholesterol (LDL-C), and very low-density lipoprotein cholesterol (VLDL-C) levels were measured by collecting the blood before sacrificing the animals. STZ-induced diabetic mice (group 1) displayed very high levels of TC, HDL, LDL, VLDL, and TG compared to the normal control group (group 6). Oral treatment with (*S*)-**7** (25 mg/kg, group 3) significantly reduced the levels of TC (−41.95 %), HDL-C (−33.08 %), LDL-C (−48.56 %), and TG (−29.43 %) compared to group 1. It also showed equivalent effects to the standard drug pioglitazone (group 2) on VLDL and TG, whereas maintaining higher the HDL-C level. Unexpectedly, oral treatment with a higher dose of (*S*)-**7** (50 mg/kg, group 4) revealed a similar reduction of the TC (−45.21 %) and HDL-C (−38.46 %) levels compared to group 3, but less reduction of the TG (−14.11 %) level; only a little improvement on the reduction of LDL-C (−55.91 %) was observed. Cotreatment of group 5 with (*S*)-**7** (25 mg/kg) and pioglitazone (30 mg/kg) produced only a better and significant reduction of the TG level compared to all other treated groups (Table 4).

Histopathological Studies of Bone, Kidney, and Liver. These studies were conducted in order to evaluate possible toxic effects of (*S*)-**7** on these tissues. In fact, it is known that the use of PPARα/γ agonists, especially if they produce a full activation, is often associated with unwanted effects such as bone fractures, renal disease, and liver dysfunction [11,45,46].

Histopathological observations of bone, kidney, and liver were carried out at 40X magnifications using hematoxylin and eosin (HE) staining. The effects of (*S*)-**7** and pioglitazone on bone, kidney, and liver tissues are shown in Figs. 11–13, respectively.

Microscopic examinations of the normal bone tissue of the non-diabetic mice revealed normal architecture of bone with normal density. By contrast, STZ-induced diabetic mice showed low bone density, which clearly indicated resorption in bone tissue (Fig. 11). However, a section of bone tissue in the treated groups 2, 3, and 5 of mice showed improvement in bone density compared to the diabetes control group; only group 4 showed a decreased level of bone density (Fig. 11).

Histopathological assessment of the normal kidney of the nondiabetic mice showed normal renal cortex, glomerular tufts, proximal tubules, and distal tubules. As expected, a kidney section of STZ-induced diabetic mice showed shrunken glomeruli and distorted proximal and distal tubules (Fig. 12). However, a kidney section of treated group 2 showed a healthy morphology of these cellular components as a clear consequence of drug effect; in group 3 only slightly shrunken glomeruli were observed, whereas groups 4 and 5 presented only a slight distortion of proximal and/or distal tubules (Fig. 12).

Histopathological assessment of the normal liver tissue of the non-diabetic mice confirmed the normal structure of the liver. Each lobule consisted of interconnecting plates of epithelial cells called hepatocytes, which were radially arranged around a central vein (Fig. 13). In contrast, liver sections of STZ-induced diabetic mice disclosed hepatocellular damage consisting in liver architectural distortion, fibrosis, inflammation, and leucocyte infiltration around the central vein (Fig. 13). Sections of the liver in diabetic rats treated with (*S*)-**7** or pioglitazone, either alone or in combination, showed an improved morphology similar to that of the healthy group (Fig. 13).

Table 3
Effect of (*S*)-**7** on fasting blood glucose levels (mg/dL) in STZ-induced diabetic mice.

Groups (n = 5)[a]	Blood glucose level (mg/dL)			
	Day 0	Day 5	Day 10	Day 15
1. diabetic control	365 ± 54.25	456.8 ± 63.77	435.2 ± 46.89	452.6 ± 48.94
2. pioglitazone	441.2 ± 35.62	351 ± 51.88	248 ± 25.97***	224.2 ± 28.28***
3. (*S*)-**7** (25 mg/kg)	336.4 ± 48.74	264.4 ± 50.93*	181.0 ± 8.82***	165.8 ± 10.96***
4. (*S*)-**7** (50 mg/kg)	424.6 ± 65.22	237.6 ± 47.28*	104.6 ± 5.84***	91.0 ± 8.73***
5. (*S*)-**7** + pioglitazone	356.4 ± 60.06	340.0 ± 33.92	169.2 ± 20.87***	105.0 ± 5.39***
6. normal control	87.6 ± 8.79	86.6 ± 8.48	86.4 ± 9.29	86.6 ± 7.77

[a] n = number of animals/group; ***$p < 0.001$ *vs* diabetic control; *$p < 0.05$ *vs* diabetic control.

Table 4
Effect of (*S*)-**7** on lipid profile in STZ-induced diabetic mice.

Blood lipid level (mg/dL)					
Groups	TC	HDL	LDL	VLDL	TG
1. diabetic control	184.33 ± 1.2	43.33 ± 1.2	113.33 ± 0.35	27.77 ± 0.15	139.33 ± 0.88
2. pioglitazone	88.67 ± 2.6***	19.67 ± 0.88***	20.50 ± 0.1***	19.33 ± 0.29	98.33 ± 0.33***
3. (*S*)-**7** (25 mg/kg)	107.00 ± 0.58***	29.00 ± 1.00***	58.30 ± 0.21***	19.50 ± 0.1	98.33 ± 0.88***
4. (*S*)-**7** (50 mg/kg)	101.00 ± 2.31***	26.67 ± 0.88***	49.97 ± 0.32***	24.20 ± 0.17	119.67 ± 2.03***
5. (*S*)-**7** + pioglitazone	93.67 ± 0.33***	25 ± 0.58***	52.50 ± 0.49***	17.60 ± 0.12	87.33 ± 0.33***
6. normal control	59.00 ± 0.58	22.33 ± 0.33	21.30 ± 0.15	15.57 ± 0.15	77.67 ± 0.88

***$p < 0.001$ vs diabetic control.

4. Conclusions

In conclusion, here we present evidence that compound *(S)*-**7** behaves as a well-tolerated antidiabetic agent, lowering blood glucose and lipids levels in diabetic mouse models. Moreover, we demonstrated that such compound behaves not only as a PPARα/γ dual agonist but also as an inhibitor of MPC. In the past, different studies demonstrated that MPC inhibition is an affordable strategy to control the energetic metabolism of cells. As shown for TZDs, this inhibition impairs pyruvate availability, reduces oxygen consumption, and mitochondrial ATP production [47]. Although it may seem counterintuitive that reduced mitochondrial pyruvate uptake may be a mechanism of insulin sensitization, it is important to note that the restriction of pyruvate-driven respiration by TZDs is never complete and is readily reversible [25]. Moreover, the reversibility of the interaction may induce a conditioning effect whereby mild, transient MPC inhibition potentiates reliance on alternative substrates. As a matter of fact, MPC disruption does not impair muscle glucose uptake; instead, it evokes complex, interconnected changes in muscle and systemic metabolism leading to increased whole-body insulin sensitivity, increased glucose uptake, and attenuation of obesity and T2D. Furthermore, MPC inhibition strongly impairs the ability of liver cells to convert pyruvate into glucose through gluconeogenesis, the metabolic pathway that often contributes to hyperglycemia in diabetic patients [48]. Taken together, this evidence suggests that MPC inhibitors can be used as antidiabetic and antilipidemic agents.

Here, we have shown that in murine myoblasts, acute treatment with

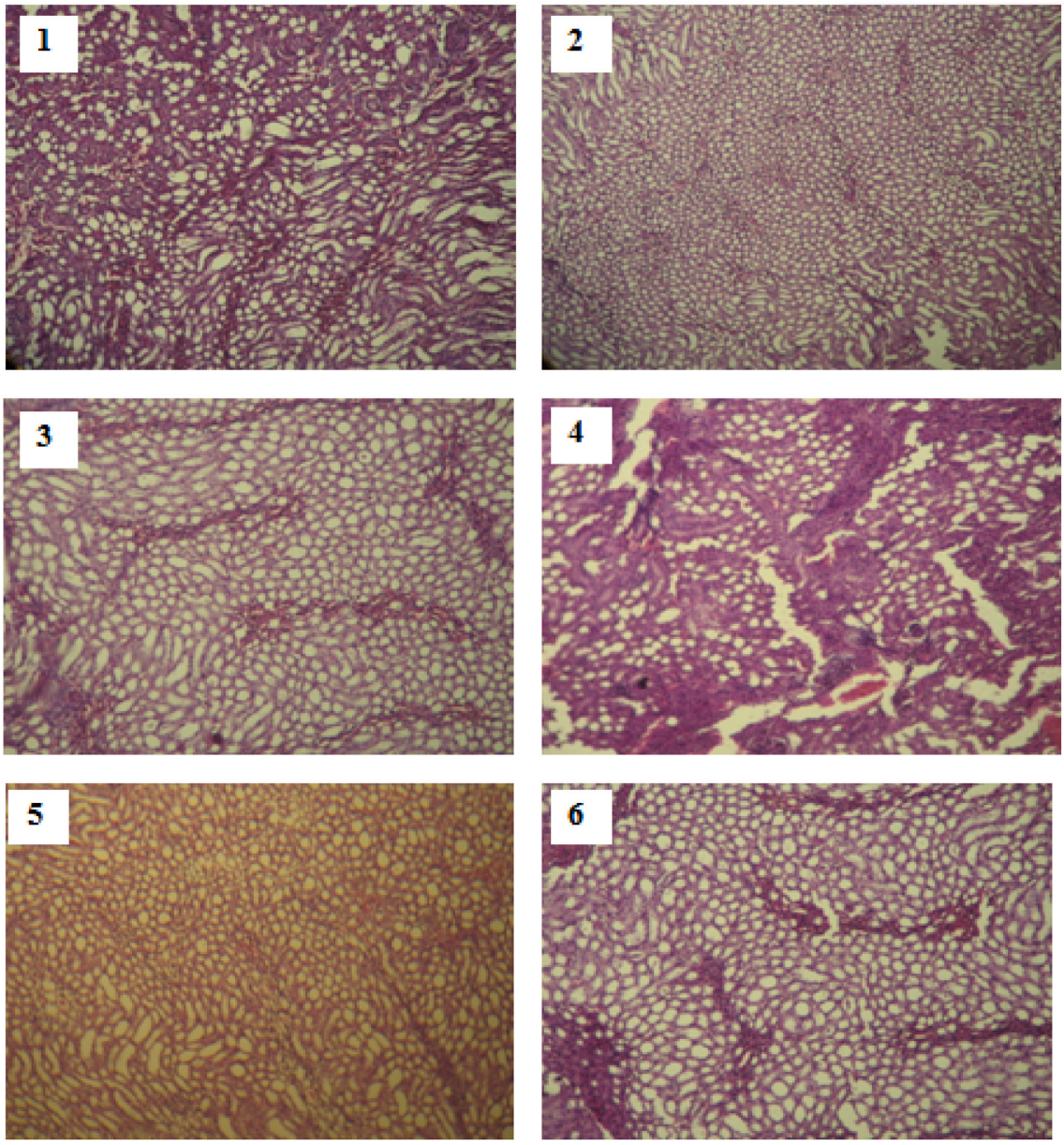

Fig. 11. Histopathology of the bone. Light micrographs of bone sections from the different groups. The numbers on the images represent the groups according to the text. Diabetic untreated group (1) revealed a marked decrease in bone density. Bone density of the treated groups 2, 3, and 5 looks healthy in comparison with the normal group (6). Only group 4 showed a decreased level of bone density. Examinations were carried out at 40X magnifications with hematoxylin–eosin staining.

(*S*)-**7** induces a rapid increase in glucose uptake, a phenomenon too rapid to be attributable to the ability of (*S*)-**7** to act as a PPAR agonist. This effect allows to hypothesize the inhibition of MPC, as demonstrated by the fact that treatment with (*S*)-**7** significantly stimulates the acidification of the external growth medium. This suggests that C2C12 cells treated with (*S*)-**7** increase the uptake and metabolism of glucose to enhance pyruvate production and try to overcome the (*S*)-**7** induced block of MPC. This block enhances pyruvate conversion to lactate and, at the same time, forces the cells to compensate the reduced entrance of pyruvate into the mitochondria by increasing oxidation of other metabolic substrates such as fatty acids and thus enhancing the OCR/ECAR ratio. Interestingly, differently from rosiglitazone, neither impaired oxygen consumption nor reduced ATP production of muscle cells was observed. This mechanism could also explain the results of (*S*)-**7** on steatosis, which show that chronic stimulation with nanomolar concentrations of (*S*)-**7** strongly reduces lipid deposits into HepG2 cells in a manner more efficient than rosiglitazone and fenofibrate. Taken together, these data confirm that (*S*)-**7** is able to increase the uptake and metabolism of glucose and enhance mitochondrial activity by boosting fatty acid degradation, thus avoiding lipid accumulation in liver or muscle cells.

The reason why the whole bioenergetics profile of C2C12 cells remained substantially unaffected after acute treatment with (*S*)-**7** could lie in the hydrophobic nature of this compound, which would favor its localization into the membrane of muscle cells. However, despite its low bioavailability, it could reach a cytoplasmic concentration sufficient to activate PPARs and to partly inhibit MPC in such a way to induce only an increase of glucose uptake without affecting other mitochondrial parameters. Obviously, it cannot be ruled out the possibility that other mechanisms occur alternatively or in concomitance with MPC inhibition. Interestingly, as regards the binding of (*S*)-**7** to PPARα and PPARγ, X-ray crystallography studies displayed binding modes typical of full agonists even though (*S*)-**7** acted only as a partial agonist. In vitro experiments as well as docking studies in the presence of PPAR antagonists

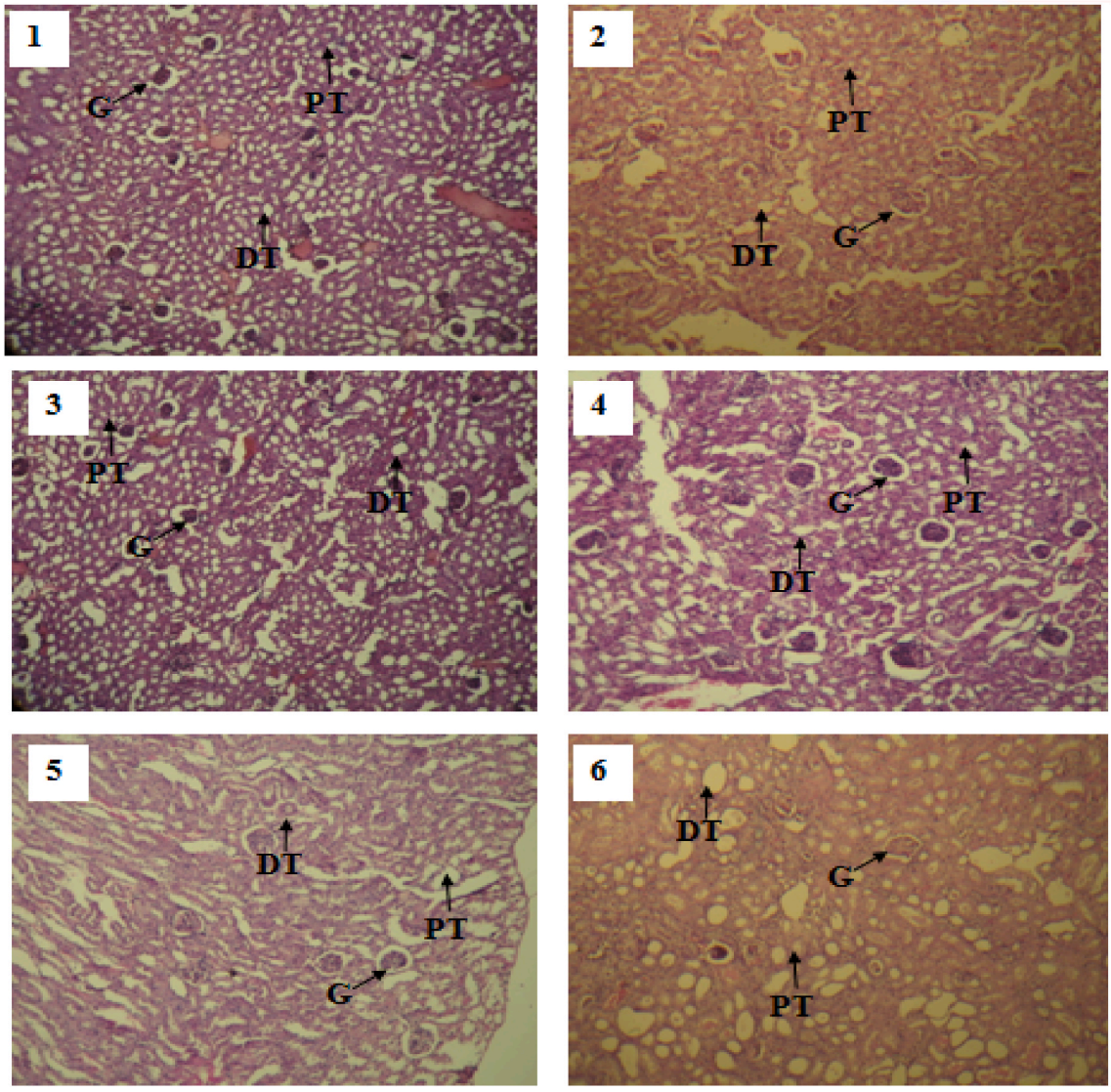

Fig. 12. Histopathology of the kidney. Light micrographs of kidney sections from the different groups. The numbers on the images represent the groups according to the text. Diabetic untreated group (1) showed shrunken glomeruli (G) and distorted proximal (PT) and distal tubules (DT). Group 2 revealed healthy conditions of G, PT, and DT; group 3 showed normal DT and PT but slightly shrunken glomeruli; groups 4 and 5 presented normal conditions of G but only a slight distortion of proximal and/or distal tubules compared to the normal group (6). Examinations were carried out at 40X magnifications with hematoxylin−eosin staining.

were performed in the attempt to give an interpretation to the biological data and investigate the main interactions at the binding sites. These studies demonstrated the complexity of the relationship between the binding mode "captured" by the crystal structure and biological activity. In fact, X-ray crystal structure corresponds only to a static representation of the possible interactions between receptor and ligand, whereas the biological activity is the result of a dynamic mechanism, which can involve the whole receptor pocket.

This work is still in progress as well as further studies to gain insight into the properties and biological action of this ligand. As far as we know, this is the first example of dual PPARα/γ partial agonist reported to show also a combined inhibitory effect on MPC. In view of its high potency towards PPARs with less efficacy and potentially reduced adverse effects, overall, (*S*)-**7** may represent a very promising candidate as the lead of a new class of drugs with better and safer therapeutic effects in the treatment of dyslipidemic type 2 diabetes.

5. Experimental Section

Chemical Methods. Chemicals were used without any further purification and purchased from common suppliers. Column chromatography was performed using Fluka silica gel 60 Å as the stationary phase. Melting points of solid compounds (uncorrected) were determined in open capillaries on a Gallenkamp electrothermal apparatus. Mass spectra were recorded on an HP MS6890-5973 MSD spectrometer equipped with an HP ChemStation or with an Agilent LC−MS 1100 Series. For exact mass analyses, in particular, we employed an LC-MSD Trap System VL spectrometer equipped with electrospray ionization (ESI). ^{1}H NMR spectra were recorded using suitable deuterated solvents on a Varian Mercury 300 NMR Spectrometer or an Agilent VNMRS 500. Chemical shifts (δ) are expressed as parts per million (ppm) and coupling constants (J) are expressed in Hertz (Hz). ^{13}C NMR (126 MHz) was recorded in DMSO-d_6 on Agilent VNMRS 500 NMR Spectrometer for (*S*)-**7** which underwent all biological assays. Optical rotations were measured with a PerkinElmer 341 polarimeter at room temperature (20 °C): concentrations are expressed as grams per 100 mL. Microanalyses of final compounds were carried out with a Eurovector Euro EA 3000 model analyzer; the analytical results are within ±0.4 % of the theoretical values. Enantio-purity of the compounds was determined by HPLC analysis carried out with a Shimadzu prominence LC-20AD liquid

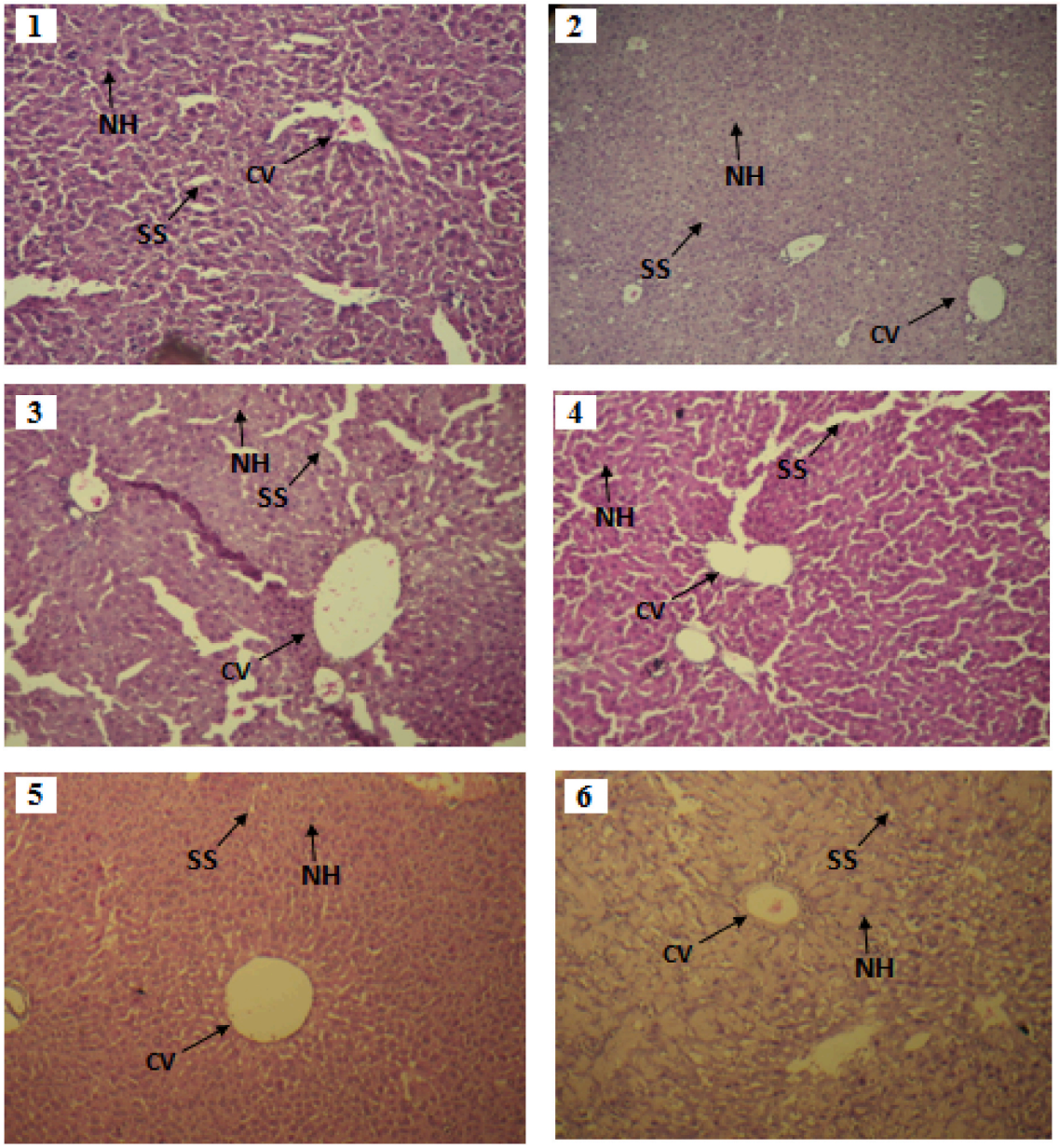

Fig. 13. Histopathology of the liver. Light micrographs of liver sections from treated and untreated groups. The numbers on the images represent the groups according to the text. Diabetic control mouse liver section (1) showing severe damaged hepatic architecture with damaged central vein (CV), elevated sinusoidal space (SS), and distorted normal hepatocytes (NH). In group 2, the pathological condition was almost back to normal. Groups 3 and 4 showed normal conditions of CV and NH surrounding CV, but slightly increased sinusoidal space. Group 5 looked healthy with normal conditions of CV, NH, and SS similar to the normal control group 6. Examinations were carried out at 40X magnifications with hematoxylin−eosin staining.

chromatograph device (Shimadzu Corporation, Tokyo, Japan) equipped with a Chiralpak IA column (5 μm particle size, 4.6 mm ⌀ × 250 mm L) (Daicel Inc., Tokyo, Japan). As mobile phase 97.0–99.5 % *n*-hexane acidified with 0.1 % trifluoroacetic acid (TFA) mixed with either 2-propanol or ethanol was applied. Solvents used are in HPLC grade (rotisolv®, Carl Roth GmbH + Co. KG, Karlsruhe, Germany). Mobile phase composition was adapted for each compound in order to achieve baseline separation of the enantiomers. Flow rate was set to 1.0 mL/min, injection volume was 5 μL (about 1 mM solutions of each compound) and the temperature was kept at 25 °C for each measurement. The purity was determined from the UV chromatogram at 300 nm and the enantiomeric excess (ee%) of the compounds was found to be >95 % except for (*S*)-**5** (ee 64.7 %).

General procedure for the synthesis of 8 and 9. KOH powder (12 mmol) was added to a solution of 4-bromo-phenol (2 mmol) in acetone or 2-butanone (6 mL). After 30 min, $CHBr_3$ (0.4 mL, 4.4 mmol) was added dropwise, during 1.5 h, to the reaction mixture. The resulting solution was stirred at room temperature overnight, then the solvent was removed under reduced pressure and the oily residue was added with distilled water and washed with $CHCl_3$. The aqueous phase was carefully acidified with 6 N HCl (until pH = 1) and extracted with chloroform. The collected organic phase was washed with brine, dried over Na_2SO_4, filtered, and evaporated to dryness, affording a brown residue which was recrystallized from *n*-hexane to give the title compounds.

2-(4-Bromophenoxy)-2-methyl-propanoic acid (***8***). Starting from acetone was obtained as a yellow solid, which was crystallized from *n*-hexane/$CHCl_3$. Yield 42 %. ^{1}H NMR (300 MHz, $CDCl_3$) δ (ppm): 1.60 (s, 6H, CH_3), 6.81–6.85 and 7.37–7.41 (m, 4H, aromatics); ESI-MS *m/z*: (IP: negative) 258.7 $[M - H]^-$.

2-(4-Bromophenoxy)-2-methyl-butanoic acid (***9***). Starting from 2-

butanone was obtained as a yellow solid. Yield = 65 %; m.p. = 100–101 °C; ^{1}H NMR (300 MHz, $CDCl_3$) δ (ppm): 1.03 (t, 3H, CH_2CH_3, J = 7.6 Hz), 1.49 (s, 3H, CH_3), 1.89–2.07 (m, 2H, CH_2), 6.81–6.86 and 7.36–7.41 (m, 4H, aromatics); GC-MS (methyl ester obtained with diazomethane) *m/z* (%): 288 (19) $[M+2]^+$, 286 (19) $[M]^+$, 229 (22), 227 (22), 174 (100).

Synthesis of diastereomeric pantolactone esters 12. To a solution of **9** (5.1 mmol) in dichloromethane (20 mL), dimethylaminopyridine (DMAP, 1.0 mmol), 1-ethyl-3-(3-dimethylaminopropyl)carbodiimide (EDCI, 6 mmol), and (*R*)-pantolactone (15.3 mmol) were added and the reaction mixture was stirred at room temperature for 24 h. Then, the organic phase was evaporated to dryness, the residue was dissolved in ethyl acetate, and washed with 1 N HCl (twice), $NaHCO_3$ and brine. The organic phase was dried over Na_2SO_4 and evaporated to dryness to afford a yellow oil. The so obtained diastereomeric esters were purified by column chromatography on silica gel using *n*-hexane/ethyl acetate 70:30 as eluent. Yield = 34 %. The two diastereomers were separated by fractional crystallization from *n*-hexane and obtained as white solids.

(R,R)-(4,4-Dimethyl-2-oxotetrahydrofuran-3-yl*) 2-(4-bromophenoxy)-2-methylbutanoate* ***((R,R)-12)***. Yield = 21 %; m.p. 86–87 °C; $[\alpha]_D$: +42.5° (c 1.0, $CHCl_3$). GC-MS *m/z* (%): 386 $[M+2]^+$ (0.8), 384 $[M]^+$ (0.9), 174 (94), 172 (100), 83 (79). ^{1}H NMR (500 MHz, $CDCl_3$): 0.95–1.06 (m, 6H, CCH_3 + CH_2CH_3), 1.16 (s, 3H, CCH_3), 1.54 (s, 3H, $OCCH_3$), 1.95–2.15 (m, 2H, CH_2CH_3), 4.03 (dd, J_1 = 10.8 Hz, J_2 = 9.3 Hz, 2H, OCH_2), 5.41 (s, 1H, CH), 6.84–6.87 and 7.33–7.37 (m, 4H, aromatics).

(R,S)-(4,4-Dimethyl-2-oxotetrahydrofuran-3-yl*) 2-(4-bromophenoxy)-2-methylbutanoate* ***((R,S)-12)***. Yield = 26 %; m.p. 137–140 °C; $[\alpha]_D$: −17.4° (c 1.0, $CHCl_3$). ^{1}H NMR (500 MHz, $CDCl_3$): 0.95 (s, 3H, CCH_3), 1.04–1.07 (m, 6H, CCH_3 + CH_2CH_3), 1.59 (s, 3H, $OCCH_3$), 2.01–2.06 (m, 2H, CH_2CH_3), 4.02 (dd, J_1 = 10.8 Hz, J_2 = 9.3Hz, 2H, OCH_2), 5.40 (s, 1H, CH), 6.78–6.80 and 7.33–7.36 (m, 4H, aromatics).

Ethyl 2-bromo-2-phenylpropanoate (14d). N-bromosuccinimide (65.27 mmol), two drops of 47 % HBr and two drops of glacial acetic acid were added to a stirred solution of ethyl 2-phenylpropanoate (27.89 mmol) in CCl_4 (30 mL). The reaction mixture was refluxed for 24 h. Then, the mixture was filtered through a Gooch funnel, added with chloroform, and washed with brine. The organic layer was dried over anhydrous Na_2SO_4, filtered, and evaporated under reduced pressure obtaining a brown oil. Yield 99 %. GC-MS *m/z* (%): 256 (0.3) $[M]^+$, 185 (27), 183 (28), 177 (100), 103 (55).

General procedure for the synthesis of compounds 15a-d. NaH (34.98 mmol) was suspended in anhydrous DMF (30 mL), then 4-bromophenol (34.98 mmol) was added under inert atmosphere at 0 °C. After 30 min a solution of the appropriate bromoester **14a-d** (17.49 mmol) in anhydrous DMF (20 mL) was added dropwise. The reaction mixture was refluxed for 6 h, then the solvent was distilled off. The residue was treated with ethyl acetate and washed with a saturated solution of NH_4Cl, 0.5 N NaOH (twice) and brine. The organic phase was dried over anhydrous Na_2SO_4, filtered, and evaporated in vacuo. The crude was purified by chromatography column (*n*-hexane/ethyl acetate 90:10 as eluent) to give the desired compounds.

Ethyl 2-(4-bromophenoxy)acetate ***(15a)***. Starting from ethyl bromoacetate **14a**, yield 57 %. ^{1}H NMR (500 MHz, $CDCl_3$) δ (ppm): 1.29 (t, J = 6.9 Hz, 3H, $COOCH_2CH_3$), 4.27 (q, J = 6.9 Hz, 2H, $COOCH_2CH_3$), 4.59 (s, 2H, OCH_2CO), 6.78–7.81 and 7.37–7.40 (m, 4H aromatics); GC-MS *m/z* (%): 260 (99) $[M+2]^+$, 258 (100) $[M]^+$, 187 (67), 185 (71), 157 (59), 76 (26).

Ethyl 2-(4-bromophenoxy)butanoate ***(15b)***. Starting from ethyl 2-bromobutanoate **14b**, the compound was obtained as a yellow oil. Yield 40 %. ^{1}H NMR (500 MHz, $CDCl_3$) δ (ppm): 1.07 (t, J = 7.4 Hz, 3H, CCH_2CH_3), 1.25 (t, J = 7.1 Hz, 3H, $COOCH_2CH_3$), 1.98 (m, 2H, CCH_2CH_3), 4.27 (q, J = 7.1 Hz, 2H, $COOCH_2CH_3$), 4.50 (t, J = 6.2 Hz, 1H, CH), 6.73–6.79 and 7.33–7.38 (m, 4H aromatics), GC-MS *m/z* (%): 288 (73) $[M+2]^+$, 286 (74) $[M]^+$, 215 (76), 213 (76), 174 (97), 172 (100).

Ethyl 2-(4-bromophenoxy)-3-methyl-butanoate ***(15c)***. Starting from ethyl 2-bromo-3-methylbutanoate **14c**, the compound was obtained as a yellow oil. Yield 51 %. GC-MS *m/z* (%): 302 (26) $[M+2]^+$, 300 (26) $[M]^+$, 229 (15), 227 (15), 174 (96), 172 (100).

Ethyl 2-(4-bromophenoxy)-2-phenyl-propanoate ***(15d)***. Starting from ethyl 2-bromo-2-phenyl-propanoate **14d**, the compound was obtained as a colorless oil. Yield 76 %. ^{1}H NMR (300 MHz, $CDCl_3$) δ (ppm): 1.16 (t, J = 7.6 Hz, 3H, CH_2CH_3), 1.87 (s, 3H, CCH_3), 4.21 (q, J = 7.6 Hz, 2H, CH_2CH_3), 6.71–6.74, 7.29–7.41 and 7.57–7.58 (m, 9H aromatics); GC-MS *m/z* (%): 348 (2) $[M]^+$, 277 (17), 275 (180), 177 (100), 103 (94).

General procedure for the synthesis of (*R*)- or (*S*)-18a-d. To a solution of (*R*)- or (*S*)-**17a-d** (3.47 mmol) in anhydrous THF (7 mL), 4-bromophenol (2.89 mmol), and triphenylphosphine (3.47 mmol) were added. Then, a solution of diisopropylazodicarboxylate (DIAD, 3.47 mmol) in anhydrous THF (4 mL) was added dropwise at 0 °C. The reaction mixture was stirred at room temperature overnight under inert atmosphere. The solvent was evaporated in vacuo, and the residue was purified by chromatography column (*n*-hexane/ethyl acetate 80:20 as eluent) to afford the desired compounds.

(S)-Methyl 2-(4-bromophenoxy)propanoate ***((S)-18a)***. Starting from (*R*)-methyl lactate (*R*)-**17a**, the compound was obtained as a white solid. Yield 42 %. GC-MS *m/z* (%): 260 (60) $[M+2]^+$, 258 (62) $[M]^+$, 201 (97), 199 (100), 174 (68), 172 (69).

(R)-Methyl 2-(4-bromophenoxy)propanoate ***((R)-18a)***. Starting from (*S*)-methyl lactate (*S*)-**17a**, the compound was obtained as a white solid. Yield 53 %.

(R)-Methyl 2-(4-bromophenoxy)butanoate ***((R)-18b)***. Starting from (*S*)-methyl 2-hydroxy-butanoate (*S*)-**17b**, which was prepared by esterification of (*S*)-2-hydroxy-butanoic acid [25] with methanol in the presence of few drops of H_2SO_4, the compound was obtained as a yellow oil. Yield 54 %. ^{1}H NMR (300 MHz, $CDCl_3$) δ (ppm): 1.06 (t, J = 7.6 Hz, 3H, CH_2CH_3), 1.43 (d, J = 6.4, 1H, CH), 1.90–2.04 (m, 2H, CH_2CH_3), 3.74 (s, 3H, OCH_3), 6.70–6.78 (m, 2H aromatics), 7.36–7.45 (m, 2H aromatics). GC-MS *m/z* (%): 274 (40) $[M+2]^+$, 272 (41) $[M]^+$, 215 (43), 213 (43), 174 (94), 172 (100).

(S)-Methyl 2-(4-bromophenoxy)butanoate ***((S)-18b)***. Starting from (*R*)-methyl 2-hydroxy-butanoate (*R*)-**17b**, which was prepared by esterification of the commercially available (*R*)-2-hydroxy-butanoic acid. Yield 50 %.

(S)-Ethyl 2-(4-bromophenoxy)-3-methyl-butanoate ***((S)-18c)***. Starting from (*R*)-ethyl 2-hydroxy-3-methyl-butanoate (*R*)-**17c**, which was prepared by esterification of (*R*)-2-hydroxy-3-methyl-butanoic acid [25], the compound was obtained as a yellow oil. Yield 30 %. GC-MS *m/z* (%): 302 (26) $[M+2]^+$, 300 (26) $[M]^+$, 229 (15), 227 (15), 174 (96), 172 (100).

(R)-Ethyl 2-(4-bromophenoxy)-3-phenyl-propanoate (**(R)-18d**). Starting from (*S*)-ethyl phenyllactate (*S*)-**17d**, the compound was obtained as a colorless oil. Yield 52 %. ^{1}H NMR (300 MHz, $CDCl_3$) δ (ppm): 1.21 (t, J = 7.6 Hz, 3H, CH_2CH_3); 3.20–3.26 (m, 2H, CH_2Ph); 4.23 (q, J = 7.6 Hz, 2H, CH_2CH_3); 4.69–4.75 (m, 1H, CH); 6.71–7.35 (m, 9H aromatics). GC-MS *m/z* (%): 348 (52) $[M]^+$, 196 (51), 135 (82), 105 (47).

(S)-Ethyl 2-(4-bromophenoxy)-3-phenyl-propanoate (**(S)-18d**). Starting from (*R*)-ethyl phenyllactate (*R*)-**17d**, the compound was obtained as a colorless oil. Yield 46 %.

5.1. General procedure for the synthesis of substituted 4-(naphthalen-1-yl)phenoxy esters 10, 11, 13, 16a-d and 19a-d

Naphthalene-1-boronic acid (2.5 mmol), Cs_2CO_3 (1.9 mmol) and water (1 mL) were added, under N_2 atmosphere, to a solution of the appropriate 4-bromo-phenoxyesters (1.2 mmol) in anhydrous toluene (22 mL). Compounds **8** and **9** were previously converted to the corresponding ethyl and methyl esters, respectively, by treatment with absolute ethanol or methanol in the presence of few drops of H_2SO_4. The mixture was stirred for 30 min at room temperature. Then, $Pd(PPh_3)_4$ (0.04 mmol) was added and the reaction mixture was refluxed for 5 h

and at room temperature overnight. The mixture was quenched with 2 N HCl and ethyl acetate (10 mL, 1:1). The catalyst was removed by filtration on a Celite pad, and the filtrate was concentrated to dryness. The crude was purified by column chromatography to give the title compounds.

Ethyl 2-methyl-2-(4-(naphthalen-1-yl*)phenoxy)propanoate* ***(10)***. Starting from ethyl 2-methyl-2-(4-bromophenoxy)propanoate, which was prepared by esterification of **8** with ethanol in the presence of H_2SO_4; eluent *n*-hexane/ethyl acetate 95:5, colorless oil. Yield 28 %. ^{1}H NMR (300 MHz, $CDCl_3$) δ (ppm): 1.29 (t, J = 6.1 Hz, 3H, OCH_2CH_3), 1.67 (s, 6H, 2 CCH_3), 4.27 (q, J = 6.1 Hz, 2H, $COOCH_2CH_3$), 6.94–6.97, 7.35–7.52 and 7.82–7.91 (m, 11H, aromatics); GC-MS *m/z* (%): 334 (38) $[M]^+$, 261 (14), 220 (100), 202 (21).

Methyl 2-methyl-2-(4-(naphthalen-1-yl*)phenoxy)butanoate* ***(11)***. Starting from methyl 2-methyl-2-(4-bromophenoxy)butanoate, which was prepared by esterification of **9** with methanol in the presence of H_2SO_4; eluent *n*-hexane/ethyl acetate 80:20. Yield 57 %. ^{1}H NMR (500 MHz, $CDCl_3$) δ (ppm): 1.04 (t, J = 7.8 Hz, 3H, CH_2CH_3), 1.60 (s, 3H, CCH_3), 2.01–2.11 (m, 2H, CH_2CH_3), 3.82 (s, 3H, OCH_3), 6.94–6.97, 7.36–7.52 and 7.82–7.91 (m, 11H, aromatics); GC-MS *m/z* (%): 334 (20) $[M]^+$, 220 (100), 189 (18).

(R,R)-(4,4-Dimethyl-2-oxotetrahydrofuran-3-yl*) 2-methyl-2-(4-(naphthalen*-1-yl*)phenoxy)butanoate* ***((R,R)-13)***. Starting from (*R,R*)-**12**, the compound was obtained as a white solid. Yield 75 %. ^{1}H NMR (300 MHz, $CDCl_3$) δ (ppm): 1.06–1.15 (m, 6H, CCH_3 + CH_2CH_3), 1.18 (s, 3H, CCH_3), 1.67 (s, 3H, $OCCH_3$), 2.04–2.30 (m, 2H, CH_2CH_3), 4.04 (dd, J_1 = 10.8 Hz, J_2 = 9.3 Hz, 2H, OCH_2), 5.47 (s, 1H, CH), 6.99–7.07, 7.36–7.52 and 7.82–7.90 (m, 11H, aromatics); GC-MS *m/z* (%): 432 (13) $[M]^+$, 275 (5), 220 (100).

(R,S)-(4,4-Dimethyl-2-oxotetrahydrofuran-3-yl*) 2-methyl-2-(4-(naphthalen*-1-yl*)phenoxy)butanoate* ***((R,S)-13)***. Starting from *(R,S)*-**12**, the compound was obtained as a white solid. Yield 66 %.%. ^{1}H NMR (300 MHz, $CDCl_3$) δ (ppm): 0.97 (s, 3H, CCH_3), 1.06–1.15 (m, 6H, CCH_3 + CH_2CH_3), 1.73 (s, 3H, $OCCH_3$), 2.04–2.30 (m, 2H, CH_2CH_3), 4.02 (s, 2H, OCH_2), 5.45 (s, 1H, CH), 6.99–7.01, 7.34–7.52 and 7.82–7.90 (m, 11H, aromatics); GC-MS *m/z* (%): 432 $[M]^+$ (13), 275 (7), 220 (100).

Ethyl 2-(4-(naphthalen-1-yl*)phenoxy)acetate* (**16a**). Starting from **15a.** Eluent *n*-hexane/ethyl acetate 90:10. Yield 80 %. ^{1}H NMR (500 MHz, $CDCl_3$) δ (ppm): 1.34 (t, J = 7.3 Hz, 3H, OCH_2CH_3), 4.32 (q, J = 7.3 Hz, 2H, OCH_2CH_3), 4.71 (s, 2H, OCH_2CO), 7.02–7.05, 7.39–7.52 and 7.83–7.91 (m, 11H, aromatics); GC-MS *m/z* (%): 306 (100) $[M]^+$, 219 (44), 202 (42).

Ethyl 2-(4-(naphthalen-1-yl*)phenoxy)butanoate* (**16b**). Starting from **15b.** Eluent *n*-hexane/ethyl acetate 90:10. Yield 48 %. ^{1}H NMR (500 MHz, DMSO-d_6) δ (ppm): 1.01 (t, J = 7.4 Hz, 3H, CH_3), 1.18 (t, J = 7.1 Hz, 3H, OCH_2CH_3), 1.86–1.96 (m, 2H, CH_2), 4.17 (q, J = 7.1 Hz, 2H, OCH_2CH_3), 4.82 (t, J = 6.0 Hz, 1H, CH), 6.97–7.02, 7.33–7.56, 7.76–7.80 and 7.87–7.98 (m, 11H, aromatics); GC-MS *m/z* (%): 334 (100) $[M]^+$, 261 (25), 220 (75).

Ethyl 3-methyl-2-(4-(naphthalen-1-yl*)phenoxy)butanoate* (**16c**). Starting from **15c**. Eluent *n*-hexane/ethyl acetate 95:5. Yield 38 %. ^{1}H NMR (500 MHz, DMSO-d_6) δ (ppm): 0.97–1.02 (m, 6H, $2CH_3$), 1.07 (t, J = 7.1 Hz, 3H, OCH_2CH_3), 2.13–2.27 (m, 1H, CH_3CHCH_3), 3.72 (q, J = 7.1 Hz, 2H, OCH_2CH_3), 4.07–4.19 (m, 1H, OCH), 6.94–7.02, 7.30–7.53, 7.65–7.77 and 7.84–7.94 (m, 11H, aromatics); GC-MS *m/z* (%): 348 (56) $[M]^+$, 275 (9), 220 (100).

Ethyl 2-(4-(naphthalen-1-yl*)phenoxy)-2-phenylpropanoate* (**16d**). Starting from **15d**. Eluent *n*-hexane/dichloromethane 50:50, yellow oil. Yield 54 %. ^{1}H NMR (300 MHz, $CDCl_3$) δ (ppm): 1.17 (t, J = 7.8 Hz, 3H, CH_2CH_3), 1.19 (s, 3H, CCH_3), 4.22 (q, J = 7.8 Hz, 2H, CH_2CH_3), 6.93–7.04, 7.30–7.57, 7.68–7.75 and 7.81–7.94 (m, 16H, aromatics).

(R)-Methyl 2-(4-(naphthalen-1-yl*)phenoxy)*propanoate ***((R)-19a)***. Starting from (*R*)-**18a.** Eluent *n*-hexane/ethyl acetate 80:20; crystallization from *n*-hexane to give a white solid. Yield 41 %. ^{1}H NMR (500 MHz, $CDCl_3$) δ (ppm): 1.68 (d, J = 6.9 Hz, 3H, $CHCH_3$), 3.82 (s, 3H, OCH_3), 4.86 (q, J = 6.9 Hz, 1H, $CHCH_3$), 6.98–7.00, 7.38–7.52 and 7.82–7.91 (m, 11H, aromatics); GC-MS *m/z* (%): 306 (100) $[M]^+$, 247 (21), 219 (90), 202 (36).

(S)-Methyl 2-(4-(naphthalen-1-yl*)phenoxy)propanoate* ***((S)-19a)***. Starting from (*S*)-**18a.** Eluent *n*-hexane/ethyl acetate 80:20; crystallization from *n*-hexane to give a white solid. Yield 14 %.

(S)-Methyl 2-(4-(naphthalen-1-yl*)phenoxy)butanoate* ***((S)-19b)***. Starting from (*S*)-**18b.** Eluent *n*-hexane/ethyl acetate 90:10, yellow oil. Yield 56 %. ^{1}H NMR (500 MHz, $CDCl_3$) δ (ppm): 1.13 (t, J = 7.4 Hz, 3H, CH_2CH_3), 2.02–2.09 (m, 2H, CH_2CH_3), 3.81 (s, 3H, OCH_3), 4.66 (t, J = 6.2 Hz, 1H, CH), 6.97–7.03, 7.38–7.43 and 7.83–7.91 (m, 11H, aromatics); GC-MS *m/z* (%): 320 (100) $[M]^+$, 261 (18), 219 (84).

(R)-Methyl 2-(4-(naphthalen-1-yl*)phenoxy)butanoate* ***((R)-19b)***. Starting from (*R*)-**18b.** Eluent *n*-hexane/ethyl acetate 90:10, yellow oil. Yield 45 %.

(S)-Ethyl 3-methyl-2-(4-(naphthalen-1-yl*)phenoxy)butanoate* ***((S)-19c)***. Starting from (*S*)-**18c.** Eluent *n*-hexane/ethyl acetate 95:5, yellow oil. Yield 70 %. ^{1}H NMR (500 MHz, DMSO-d_6) δ (ppm): 0.97–1.02 (m, 6H, CH_3CHCH_3), 1.07 (t, J = 7.1 Hz, 3H, OCH_2CH_3), 2.13–2.27 (m, 1H, CH_3CHCH_3), 3.72 (q, J = 7.1 Hz, 2H, OCH_2CH_3), 4.07–4.19 (m, 1H, OCH), 6.94–7.02, 7.30–7.53, 7.65–7.77 and 7.84–7.94 (m, 11H, aromatics). GC-MS *m/z* (%): 348 (56) $[M]^+$, 275 (9), 220 (100).

(R)-Ethyl 2-(4-(naphthalen-1-yl*)phenoxy)-3-phenyl-propanoate* ***((R)-19d)***. Starting from (*R*)-**18d.** Eluent *n*-hexane/ethyl acetate 80:20, brown oil. Yield 62 %. ^{1}H NMR (500 MHz, $CDCl_3$) δ (ppm): 1.24 (t, J = 7.12 Hz, 3H, OCH_2CH_3), 3.23–3.38 (m, 2H, $CHCH_2Ph$), 4.24 (q, J = 7.12 Hz, 2H, OCH_2CH_3), 4.89 (dd, J_1 = 7.89 Hz, J_2 = 5.16 Hz, 1H, OCH), 6.93–7.01, 7.24–7.55 and 7.78–7.93 (m, 16H, aromatics); GC-MS *m/z* (%): 396 (100) $[M]^+$, 219 (42), 135 (35), 105 (47).

(S)-Ethyl 2-(4-(naphthalen-1-yl*)phenoxy)-3-phenyl-propanoate* ***((S)-19d)***. Starting from (*S*)-**18d.** Eluent *n*-hexane/ethyl acetate 80:20, brown oil. Yield 71 %.

5.2. Synthesis of final compounds R-3 and S-3. General procedure

2.5 N NaOH (5 mL) was added to a solution of (*R,R*)-**13** or (*R,S*)-**13** (0.24 mmol) in 2-propanol (5 mL) and the reaction mixture was refluxed overnight. Next, the organic solvent was removed under reduced pressure, the aqueous residue was acidified with 2 N HCl and then extracted with acetyl acetate (three times). The collected organic portions were washed with brine, dried over anhydrous Na_2SO_4, filtered, and concentrated to dryness obtaining an oil, which was converted to the corresponding cyclohexylamine salt.

5.2.1. (R)-2-Methyl-2-(4-(naphthalen-1-yl)phenoxy)butanoate, cyclohexylammonium salt ***((R)-3)***

Starting from (*R,R*)-**13**, the compound was obtained as a white solid; $[\alpha]_D$ = +12.38 (c 1.01, CH_2Cl_2); *ee* = 97.2 % (Chiralpak IA column, 99.4 % *n*-hexane (TFA 0.1 %) and 0.6 % EtOH as a mobile phase, flow rate: 1.0 mL/min, detection 300 nm). ^{1}H NMR (500 MHz, $CDCl_3$) δ (ppm): 0.99 (t, J = 7.3 Hz, 3H, CH_2CH_3), 1.02–1.52 (m, 6H, 3 CH_2 of cyclohexylamine), 1.52 (s, 3H, CH_3), 1.67–1.70 (m, 2H, 1 CH_2 of cyclohexylamine), 1.88–2.07 (m, 4H, CH_2 of cyclohexylamine + CH_2CH_3), 2.63–2.66 (m, 1H, cyclohexylamine CH), 6.99–7.01, 7.32–7.47 and 7.80–7.90 (m, 11H, aromatics). HRMS ($C_{21}H_{20}O_3$–H^-): calculated 319.1340, found 319.1370.

5.2.2. (S)-2-Methyl-2-(4-(naphthalen-1-yl)phenoxy)butanoate, cyclohexylammonium salt ***((S)-3)***

Starting from (*R,S*)-**13**, the compound was obtained as a white solid; $[\alpha]_D$ = −13.3 (c 0.97, CH_2Cl_2); *ee* = 96.9 % (Chiralpak IA column, 99.4 % *n*-hexane (TFA 0.1 %) and 0.6 % EtOH as a mobile phase, flow rate: 1.0 mL/min, detection 300 nm). HRMS ($C_{21}H_{20}O_3$–H^-): calculated 319.1340, found 319.1359.

General procedure for the synthesis of final compounds AL-29–26, 1, (*R*)-2, (*S*)-2, (*R,S*)-3, (*R,S*)-4, (*R*)-4, (*S*)-4, (*R,S*)-5, (*S*)-5, (*R, S*)-6, (*R*)-7, (*S*)-7. 2 N NaOH (6.5 mL) was added to a solution of the

appropriate esters (1.3 mmol) in THF (6.5 mL). The resulting mixture was stirred at room temperature for 4 h. Next, the organic solvent was removed under reduced pressure, the aqueous residue was washed with ethyl acetate and then acidified with 2 N HCl. The aqueous layer was extracted with ethyl acetate (three times). The collected organic portions were washed with brine, dried over anhydrous Na_2SO_4, filtered, and concentrated to dryness.

2-Methyl-2-(4-(naphthalen-1-yl*)phenoxy)propanoic acid* (***AL29-26***). Starting from **10**. Crystallization from *n*-hexane/$CHCl_3$ gave a white solid. Yield 77 %; m.p. 131.6–132 °C. ^{1}H NMR (300 MHz, $CDCl_3$) δ (ppm): 1.68 (s, 6H, $2CH_3$), 7.06–7.91 (m, 11H, aromatics); HRMS ($C_{20}H_{18}O_3$–H^-): calculated 305.1183, found 305.1105.

2-(4-(Naphthalen-1-yl*)phenoxy)acetic acid* (***1***). Starting from **16a**. Crystallization from *n*-hexane/$CHCl_3$ gave a white solid. Yield 50 %; m.p. 207.0–208.0 °C. ^{1}H NMR (500 MHz, $CDCl_3$) δ (ppm): 4.77 (s, 2H, CH_2), 7.05–7.07, 7.38–7.52 and 7.83–7.91 (m, 11H, aromatics); HRMS ($C_{18}H_{14}O_3$–H^-): calculated 277.0870, found 277.0868.

(S)-2-(4-(Naphthalen-1-yl*)phenoxy)propanoic acid* (***(S)-2***). Starting from (*S*)-**19a**. Crystallization from *n*-hexane gave a white solid. Yield 44 %; m.p. 108–112 °C; *ee* = 99.9 % (Chiralpak IA column, 99 % *n*-hexane (TFA 0.1 %) and 1.0 % EtOH as a mobile phase, flow rate: 1.0 mL/min, detection 300 nm). ^{1}H NMR (300 MHz, $CDCl_3$) δ (ppm): 1.67 (d, J = 7.0 Hz, 3H, CH_3), 4.88 (q, J = 7.0 Hz, 1H, CH), 7.01–7.03, 7.35–7.51 and 7.81–7.89 (m, 11H, aromatics). HRMS ($C_{19}H_{16}O_3$–H^-): calculated 291.1027, found 291.1038.

(R)-2-(4-(Naphthalen-1-yl*)phenoxy)propanoic acid* (***(R)-2***). Starting from (*R*)-**19a**. Crystallization from *n*-hexane gave a white solid. Yield 44 %; m.p. 109–112 °C; *ee* = 99.9 % (Chiralpak IA column, 99 % *n*-hexane (TFA 0.1 %) and 1.0 % EtOH as a mobile phase, flow rate: 1.0 mL/min, detection 300 nm). HRMS ($C_{19}H_{16}O_3$–H^-): calculated 291.1027, found 291.1042.

2-Methyl-2-(4-(naphthalen-1-yl*)phenoxy)butanoate* (***(R,S)-3***). Starting from **11**. Crystallization from *n*-hexane gave a white solid. Yield 30 %. ^{1}H NMR (500 MHz, $CDCl_3$) δ (ppm): 1.10 (t, J = 7.3 Hz, 3H, CH_2CH_3), 1.58 (s, 3H, $C\underline{CH_3}$), 1.97–2.11 (m, 2H, CH_2CH_3), 7.05–7.07, 7.36–7.50 and 7.83–7.90 (m, 11H, aromatics); HRMS ($C_{21}H_{20}O_3$–H^-): calculated 319.1340, found 319.1306.

2-(4-(Naphthalen-1-yl*)phenoxy)butanoic acid* (***(R,S)-4***). Starting from **16b**. Crystallization from *n*-hexane/$CHCl_3$ gave a white solid. Yield 63 %. ^{1}H NMR (300 MHz, $CDCl_3$) δ (ppm): 1.16 (t, J = 7.4 Hz, 3H, CH_3), 1.99–2.05 (m, 2H, CH_2), 4.68–4.73 (m, 1H, CH), 7.42–7.52 and 7.80–7.88 (m, 11H, aromatics); HRMS ($C_{20}H_{18}O_3$–H^-): calculated 305.1183, found 305.1185.

(R)-2-(4-(Naphthalen-1-yl*)phenoxy)butanoate cyclohexylammonium salt* (***(R)-4***). Starting from (*R*)-**19b**. The compound was purified as cyclohexylamine salt to give a white solid. Yield 80 %; *ee* = 95.9 % (Chiralpak IA column, 99.5 % *n*-hexane (TFA 0.1 %) and 0.5 % EtOH as a mobile phase, flow rate: 1.0 mL/min, detection 300 nm). ^{1}H NMR (500 MHz, DMSO-d_6) δ (ppm): 0.96 (t, J = 7.3 Hz, 3H, CH_3), 1.00–1.24 (m, 4H, 2 cyclohexylamine CH_2), 1.51–1.54 (m, 2H, cyclohexylamine CH_2), 1.64–1.66 (m, 2H, cyclohexylamine CH_2), 1.71–1.84 (m, 4H, cyclohexylamine CH_2 + CH_2CH_3), 2.72–2.76 (m, 1H, cyclohexylamine CH), 4.09–4.15 (m, 1H, CH), 6.88–6.94, 7.23–7.39, 7.43–7.56 and 7.82–7.99 (m, 11H, aromatics). HRMS ($C_{20}H_{18}O_3$–H^-): calculated 305.1183, found 305.1230.

(S)-2-(4-(Naphthalen-1-yl*)phenoxy)butanoate cyclohexylammonium salt* (***(S)-4***). Starting from (*S*)-**19b**. The compound was purified as cyclohexylamine salt to give a white solid. Yield 68 %; *ee* = 99.9 % (Chiralpak IA column, 99.5 % *n*-hexane (TFA 0.1 %) and 0.5 % EtOH as a mobile phase, flow rate: 1.0 mL/min, detection 300 nm). ^{1}H NMR (500 MHz, $CDCl_3$) δ (ppm): 1.10 (t, J = 7.3 Hz, 3H, CH_3), 1.23–1.37, 1.50–1.55, 1.63–1.73 and 1.92–2.08 (m, 12H, 5 cyclohexylamine CH_2 + CH_2CH_3), 2.74–2.84 (m, 1H, cyclohexylamine CH), 4.66 (t, J_1 = 7.7 Hz, J_2 = 4.5 Hz, 1H, CH), 6.95–7.03, 7.31–7.49 and 7.80–7.90 (m, 11H, aromatics). HRMS ($C_{20}H_{18}O_3$–H^-): calculated 305.1183, found 305.1224.

3-Methyl-2-(4-(naphthalen-1-yl*)phenoxy)butanoic acid* (***(R,S)-5***). Starting from **16c**. The crude was converted to cyclohexylamine salt and then treated with 1 N HCl to give the final free acid as a white solid. Yield 10 %. ^{1}H NMR (300 MHz, DMSO-d_6) δ (ppm): 1.17 (d, J = 6.6 Hz, 6H, $2CH_3$), 2.34–2.43 (m, 1H, CH_3CHCH_3), 4.55 (d, J = 4.89 Hz, 1H, OCH), 7.02–7.06, 7.37–7.51 and 7.82–7.90 (m, 11H, aromatics). HRMS ($C_{21}H_{20}O_3$–H^-): calculated 319.1340, found 319.1315.

(S)-3-Methyl-2-(4-(naphthalen-1-yl*)phenoxy)butanoic acid* (***(S)-5***). Starting from (*S*)-**19c**. The compound was crystallized from *n*-hexane to give a white solid. Yield 10 %; *ee* = 64.7 % (Chiralpak IA column, 99.5 % *n*-hexane (TFA 0.1 %) and 0.5 % EtOH as a mobile phase, flow rate: 1.0 mL/min, detection 300 nm). ^{1}H NMR (300 MHz, $CDCl_3$) δ (ppm): 1.16 (d, J = 2.93 Hz, 3H, CH_3), 1.18 (d, J = 2.35 Hz, 3H, CH_3), 2.37–2.42 (m, 1H, CH_3CHCH_3), 4.56 (d, J = 4.68 Hz, 1H, OCH), 7.03–7.05, 7.40–7.43, 7.37–7.52 and 7.83–7.89 (m, 11H, aromatics); HRMS ($C_{21}H_{20}O_3$–H^-): calculated 319.1340, found 319.1336.

2-(4-(Naphthalen-1-yl*)phenoxy)-2-phenyl-propanoic acid* (***(R,S)-6***). Starting from **16d**. The compound was crystallized from *n*-hexane/$CHCl_3$ to give a white solid. Yield 56 %; m.p. 120–121 °C. ^{1}H NMR (300 MHz, $CDCl_3$) δ (ppm): 2.02 (s, 3H, CH_3), 6.93–6.96, 7.32–7.51, 7.66–7.68 and 7.82–7.90 (m, 16H, aromatics); HRMS ($C_{25}H_{20}O_3$–H^-): calculated 367.1340, found 367.1330.

(R)-2-(4-(Naphthalen-1-yl*)phenoxy)-3-phenyl-propanoic acid* (***(R)-7***). Starting from (*R*)-**19d**. The compound was obtained as a white solid. Yield 44 %; *ee* = 99.8 % (Chiralpak IA column, 98.0 % *n*-hexane (TFA 0.1 %) and 2.0 % isopropanol as a mobile phase, flow rate: 1.0 mL/min, detection 300 nm). ^{1}H NMR (300 MHz, DMSO-d_6) δ (ppm): 2.99 (dd, 1H, J_1 = 14.1 Hz, J_2 = 10.0 Hz, 1H, $CHCH_2Ph$), 3.18 (dd, J_1 = 14.1 Hz, J_2 = 2.8 Hz, 1H, $CHCH_2Ph$), 4.38 (dd, J_1 = 10.0 Hz, J_2 = 2.8 Hz, 1H, OCH), 6.85–6.93, 7.10–7.60, and 7.78–7.99 (m, 16H, aromatics). HRMS ($C_{25}H_{20}O_3$–H^-): calculated 367.1340 found 376.1332.

(S)-2-(4-(Naphthalen-1-yl*)phenoxy)-3-phenyl-propanoic acid* (***(S)-7***). Starting from (*S*)-**19d**. The compound was obtained as a white solid. Yield 85 %; *ee* = 98.5 % (Chiralpak IA column, 98.0 % *n*-hexane (TFA 0.1 %) and 2.0 % isopropanol as a mobile phase, flow rate: 1.0 mL/min, detection 300 nm). ^{13}C NMR: 173.97, 158.88, 140.39, 139.95, 133.91, 131.51, 131.49, 130.78, 129.61, 128.71, 128.45, 127.49, 127.11, 126.56, 126.27, 126.24, 126.02, 125.88, 115.22, 80.98. HRMS ($C_{25}H_{20}O_3$–H^-): calculated 367.1340, found 376.1321.

Preparation of (+)-(*R*)-9 from (+)-12 (Scheme 3). A solution of the pantolactone ester (+)-**12** (90 mg) in 2-propanol (5 mL) was added with 2.5 N NaOH (5 mL) and the mixture was warmed at 65 °C overnight. Then, the organic solvent was removed under reduced pressure, the aqueous residue was acidified with 2 N HCl and extracted with acetyl acetate (three times). The collected organic layers were washed with brine, dried over anhydrous Na_2SO_4, filtered, and concentrated to dryness affording the title compound as a solid (60 mg). $[\alpha]_D$ = + 16.5 (c 1.0, MeOH).

PPAR Protein Expression and Purification. PPARγ-LBD and PPARα-LBD were expressed as N-terminal His-tagged proteins using a pET28a vector and then purified as previously described [49]. Briefly, freshly transformed *E. coli* BL21 (DE3) were grown in LB medium with 50 μg of kanamycin mL^{-1} at 310 K to an OD_{600} of 0.6. The culture was then induced with 0.2 mM isopropyl-β-D-thiogalactopyranoside and further incubated at 291 K for 20 h. Cells were harvested and resuspended in Buffer A (20 mM Tris, pH 8.0, 150 mM NaCl, 10 % v/v glycerol, 1 mM TCEP) in the presence of protease inhibitors (Complete EDTA-free; Roche Applied Science). Cells were sonicated, and the soluble fraction was isolated by centrifugation. The supernatant was loaded onto a Nickel NTA agarose bulk resin (ABT) and eluted with a gradient of imidazole 10–300 mM in Buffer A (batch method). The pure proteins were identified by SDS−PAGE. The proteins were then dialyzed over buffer A to remove imidazole and cleaved with thrombin protease (GE Healthcare) (10 units mg^{-1}) at room temperature for 2 h. The digested mixture was reloaded onto a Nickel NTA agarose bulk resin (ABT) column to remove His-tags and the undigested protein. The flow-through

was dialyzed with Buffer B (20 mM Tris, pH 8.0, 10 % v/v glycerol, 1 mM TCEP) to remove NaCl and then loaded onto a Q-Sepharose HP column (GE Healthcare) and eluted with a gradient of NaCl 0−500 mM in Buffer B with a BioLogic DuoFlow FPLC system (Bio-Rad Laboratories). Finally, the proteins were purified by gel-filtration chromatography on a HiLoad Superdex 75 column (GE Healthcare) and eluted with buffer C (20 mM Tris, pH 8.0, 1 mM TCEP, 0.5 mM EDTA). The proteins were then concentrated at 8.0 mg mL^{-1} using Amicon centrifugal concentrators (Millipore) with a 10 kDa cutoff membrane.

Crystallization and Data Collection. Crystals of apo-PPARγ (0.2 × 0.2 mm) were obtained by vapor diffusion at 18 °C using a sitting drop made by mixing 2 μL of protein solution with 2 μL of reservoir solution (0.8 M Na Citrate, 0.15 M Tris, pH 8.0). The crystals were soaked for few days in a storage solution (1.2 M Na Citrate, 0.15 M Tris, pH 8.0) containing the ligand (*S*)-**7** (0.5 mM). The ligand was dissolved in DMSO (50 mM) and diluted in the storage solution so that the final concentration of DMSO was 1 %. The storage solution with glycerol 20 % (v/v) was used as cryoprotectant. The crystals of PPARγ-LBD belong to the space group C2 with cell parameters shown in Table 1 of Supporting Information.

Crystals apo-PPARα (0.7 × 0.2 mm) were obtained by vapor diffusion at 18 °C using a sitting drop made by mixing 2 μL of protein solution with 2 μL of reservoir solution (20 % PEG 3350, 0.2 M Mg Acetate). The crystals were soaked for few days in a storage solution (24 % PEG3350, 0.2 M Mg Acetate) containing the ligand (*S*)-**7** (0.5 mM). The ligand was dissolved in DMSO (50 mM) and diluted in the storage solution so that the final concentration of DMSO was 1 %. The storage solution with glycerol 20 % (v/v) was used as cryoprotectant. The crystals of PPARα-LBD belong to the space group $P4_12_12$ with cell parameters shown in Table 1 of Supporting Information.

Structure Determination and Refinement. X-ray data set were collected at 100 K under a nitrogen stream using sinchrotron radiation (beamline ID 30A-3 at ESRF, Grenoble, France). For PPARγ-LBD, the collected data were processed using the program autoPROC [50]. Structure solution was performed with AMoRe [51] by using the coordinates of the PDB entry 2P4Y as the starting model. The coordinates were then refined with CNS [52] including all data between 50.79 and 3.14 Å.

For PPARα-LBD, the collected data were processed using the program XDS [53]. Structure solution was performed with AMoRe by using the coordinates of the PDB entry 5HYK as the starting model. The coordinates were then refined with CNS including all data between 55.79 and 3.10 Å. For both PPARγ and PPARα-LBD, a final step of refinement was performed with the software Phenix [54]. The statistics of crystallographic data for both complex structures and refinement are summarized in Table 1 of Supporting Information.

Computational Chemistry. *Protein and Ligand Preparation.* The X-ray structure of PPARγ LBD in complex with **20** and arachidonic acid (PDB 6MD2) at 2.2 Å resolution [34] and of PPARα LBD in complex with **20** and fenofibric acid (PDB 6L36) at 3.3 Å resolution [41] were downloaded from the Protein Data Bank. The Protein Preparation Wizard in Maestro (Protein Preparation Wizard; Epik, Schrodinger, LLC, New York, NY, 2021; Impact, Schrodinger, LLC, New York,NY, 2021; Prime, Schrodinger, LLC, New York, NY, 2021) was used to prepare the selected structures for molecular modeling studies: all the crystallographic water molecules and other chemical components were removed; the right bond orders, charges, and atom types were assigned; and the hydrogen atoms were added. Missing side chains and incomplete protein loops were fixed. The H-bond network was optimized by exhaustive sampling of rotamers, tautomers, and protonation states of titratable amino acids at neutral pH. Finally, a restrained minimization was performed on the protein structures using the Impref module, by imposing a 0.3 Å RMSD limit from the initial coordinates as constraint. Compounds under study were drawn using Maestro 2D Sketcher and prepared with LigPrep (LigPrep, Schrodinger, LLC, New York, NY, 2021) to generate suitable 3D conformations and tautomerization states at pH 7.

Docking Calculations. Docking of the compounds under study was carried out with Glide module (Glide, Schrödinger, LLC, New York, NY, 2021) [33]. The docking grid was generated by considering a box of 15 Å × 15 Å × 15 Å surrounding the bound arachidonic acid in the case of PPARγ, and fenofibric acid in the case of PPARα. The lowest-energy values of the GlideScore function were considered for final pose selection. To remove any residual geometric strain, the obtained complexes were energy-minimized by means of MacroModel (MacroModel, Schrodinger, LLC, New York, NY, 2021), using the OPLS4 force field with steepest descent (100 iterations) followed by Polak−Ribiere conjugate gradient methods (2500 iterations).

Molecular Dynamics Simulations. The protein-ligand complexes obtained by the above-described docking procedures were selected for molecular dynamics simulations, carried out by means of Desmond [40]. Briefly, the system was solvated in a 10 Å layer orthorhombic box using TIP3P water model, and then neutralized by adding counterions. A salt concentration of 0.15 M of NaCl was also included in the simulation box to reproduce the physiological conditions. OPLS4 was used as force field [55]. The system was relaxed before the simulation by using the protocol implemented in Desmond, involving eight steps. The first seven steps consisted of short simulations to gradually increase the temperature and decrease restraints on the solute, aiming to reach an equilibrated state. Then, for the equilibrated system, the simulation was run for 100 ns under a NTP ensemble using the Nose-Hoover thermostat to maintain a constant temperature of 310 K and Martyna-Tobias-Klein barostat to maintain the pressure at 1 atm. The trajectories were saved at 100 ps intervals for analysis. The "Simulation Interactions Diagram" tool was then used for post-MD analysis. The stability of MD simulations was monitored by observing the root mean square deviation (RMSD) of the ligand and protein atom over simulation time. All the figures were rendered with PyMOL (The PyMOL Molecular Graphics System, Version 2.0 Schrodinger, LLC).

Biological Experiments. *Cell culture*. Human liver cells (HepG2) and murine myoblasts (C2C12 cells) were purchased from American Type Culture Collection (ATCC, USA) or Interlab Cell Line Collection, Genoa, Italy. Cells were maintained in Dulbecco's Modified Eagle's medium (DMEM) supplemented with 10 % Fetal Bovine Serum (FBS), 2 mM glutamine, 100 U/mL penicillin G, 100 μg/mL streptomycin (Merck Life Science S.r.l., Italy).

PPAR Assay. Reference compounds, the cell culture medium, and other reagents were purchased from Sigma-Aldrich (Milan, Italy). The expression vectors bearing the chimeric receptor containing the yeast Gal4-DNA-binding domain fused to the human PPARα- or PPARγ-LBD, and the reporter plasmids for these Gal4 chimeric receptors (pGal5TKpGL3), comprising five repeats of the Gal4 response elements upstream of a minimal thymidine kinase promoter adjacent to the coding sequence for luciferase, were described in a previous work [26a]. A culture of the human hepatoblastoma cell line HepG2 was conducted in minimum essential medium (MEM) containing 10 % heat-inactivated fetal bovine serum, 100 U/mL of penicillin G, and 100 μg/mL of streptomycin sulfate at 37 °C in a humidified atmosphere of 5 % CO_2. For transactivation assays, cells were seeded in a 24-well plate at a concentration of 10^5 cells per well and were transfected after 24 h with CAPHOS, a calcium phosphate method, according to the manufacturer's guidelines. Cell transfection was performed using expression plasmids encoding the fusion protein Gal4-PPARα-LBD or Gal4-PPARγ-LBD (30 ng), pGal5TKpGL3 (100 ng), and pCMVβgal (250 ng). Following transfection, cells were incubated for 4 h, after which they underwent treatment with the indicated ligands in triplicate for 20 h. For studies involving the covalent antagonists **20** and **21**, before incubation with ligands (*S*)-**7** and pioglitazone, cells were first preincubated with 5 μM **20** or **21** for 3 h. Cell extracts were subsequently analyzed for luciferase activity via luminometry (VICTOR [3] V multilabel plate reader, PerkinElmer). *Ortho*-nitrophenyl-β-D-galactopyranoside was used to measure β- Galactosidase activity, following a previously described method [56]. All transfection experiments were performed at least twice.

Lipid accumulation. HepG2 cells (50,000 cells for each well) were seeded in 24 well plates. The day after, liver cells were incubated with starvation medium containing or not 1 mM oleic acid. After 24 h incubation, the medium was withdrawn and replaced with fresh starvation medium containing 100 nM (*S*)-**7**, 10 μM rosiglitazone or 250 μM fenofibrate. Cells were stored at 37 °C for 72 h before to evaluate their lipid content using Oil Red staining method. Oil Red O stock solution was prepared by dissolving 0.2 g of dye in 40 mL of 2-propanol (0.5 % w/v). The working solution was obtained by diluting the stock solution 2:3 with distilled water, obtaining a concentration of 0.2 % Oil Red O in 40 % 2-propanol. The working solution was prepared fresh for each experiment and was filtered immediately before use. HepG2 cells were seeded into 24 MW plates and stored at 37 °C for 24 h. The next day, the growth medium was removed from the plate and the cells were washed with phosphate buffered saline (PBS). Then, the cells were incubated with 250 μL of 60 % 2-propanol solution for 5 min and then for 30 min with 500 μL of Oil Red O working solution. After this time the solution was removed, and the plates were washed 5 times with distilled water. To elute dye binding to intracellular lipids, 500 μL/well of 100 % 2-propanol were added to each set of plates which were then incubated for 10 min at room temperature on an orbital shaker. Next, 200 μL of eluate was transferred to a transparent 96-well microtiter plate (polystyrene) and analyzed using the iMark™ microplate reader (Biorad), measuring the absorbance of the solution at 510 nm. Each experiment was conducted in quadruplicate. After reading, each plate was washed with distilled water until the dye was completely removed. Next, 300 mL of Bradford reagent (Sigma Aldrich) was added to each plate. The plates were incubated at room temperature for 10 min and then washed with water. The plate was scanned, and the various wells were analyzed with ImageJ to quantify the amount of protein present in each well. Finally, the data obtained from the Oil Red O test were normalized for protein content. All data were normalized to the control experiment.

Seahorse Xfe96 Metabolic Assays. C2C12 cells (15,000 cells for each well) were seeded in XFe96 cell culture plates in complete growth medium. Ten hours after seeding, the complete growth medium was withdrawn and replaced with starvation medium containing or not 100 nM (*S*)-**7** or 10 μM rosiglitazone. Cells were stored overnight at 37 °C. The day after, cells were stimulated with 10 nM insulin for 30 min and then washed with fresh PBS. After washing, cells were incubated in the presence of XF base medium supplemented with 2 mM glutamine, 1 mM sodium pyruvate, and 25 mM glucose and stored in a non-CO_2 incubator for 1 h at 37 °C. The XF Mito Stress Test was performed according to the manufacturer's instructions. All data obtained were normalized for the protein content. Eight technical replicates were carried out for each condition.

Glucose uptake assay. C2C12 myoblasts were seeded on 24-well plates, starved for 24 h and then stimulated for 30 min with 50 μM (*S*)-**7** or 10 nM insulin or the combination (*S*)-**7**−insulin. After stimulation, starvation medium was removed, cells were washed with PBS and then incubated for 3 h at 37 °C with 40 μM 2-NBDG dissolved in starvation medium. After this time, C2C12 cells were trypsinized, collected in conical tubes, centrifuged, and washed with PBS. Then, the samples were analyzed using a BD FACS Canto II analyzer to evaluate the amount of fluorescent glucose loaded by the muscle cells. All tests were carried out in triplicate. Data obtained were normalized with respect to the control sample and reported as the mean ± SD.

In Vivo Pharmacokinetic Study of Compound (*S*)-7. *Chemicals and Reagents*. MS-grade (≥99.0 % pure) ammonium formate and formic acid were sourced from Sigma-Aldrich. HPLC-grade acetoni-trile, methanol, isopropyl alcohol, and dimethyl sulfoxide solvents were purchased from Merck Germany. Milli-Q Water used for the preparation of the mobile phase, rinsing solvent, and seal washes was obtained from the in-house (Eurofins Advinus Limited) Milli-Q system. The internal standard warfarin ($C_{19}H_{16}O_4$, 308.33, purity ≥97 %) used in the study was procured from Sigma-Aldrich. Male Sprague−Dawley rats (220−240 g) were obtained from Hylasco Biotechnology (India) Pvt., Ltd. (subsidiary of Charles River from USA). A SCIEX API 6500 + LC/MS/MS triple-quadrupole mass spectrometer system equipped with a negative ESI source and Shimadzu prominence HPLC comprising of binary pumps, a column oven, and an SIL-HTC autosampler was used in the study. Data acquisition, integration, and quantification were performed using Analyst 1.6.3.

Chromatographic and Mass Spectrometric Conditions. Liquid chromatographic separations of compound (*S*)-**7** and internal standard, warfarin, were achieved on a reversed-phase Kinetex EVO C18, 100 × 4.6 mm, 2.6 μm column operating at 40 °C. The isocratic mobile phase was a 20:80 (v/v) mixture of 10 mM ammonium formate containing 0.1 % formic acid (mobile phase A) and 0.1 % formic acid in acetonitrile (mobile phase B) delivered at a flow rate of 0.8 mL/min without a splitter. The mass spectrometer was operated in negative ESI mode with unit mass resolution in a quadrupole analyzer with 200 ms dwell time, and the analytes were detected by multiple reaction monitoring (MRM). The compound parameters of (*S*)-**7** and warfarin (internal standard) were optimized along with the MRM transition (*m/z*) to achieve sensitivity. Source parameters were optimized to a curtain gas N_2 flow of 30 psi (CUR), nebulizer N_2 gas of 40 psi (gas 1), ion spray voltage of −4500 V (IS), auxiliary N_2 gas of 50 psi (gas 2) with a turbo spray temperature of 550 °C (TEMP), and collision-activated dissociation gas (CAD) of 8 psi. MRM transition (*m/z*) selected for the analyte (*S*)-**7** was 367.1 → 169.1, and that for warfarin (internal standard) was 307.1 → 160.9. A system suitability test was performed prior to analysis of samples. The system suitability test comprised six replicate injections of extracted ULOQ and an extracted blank and LLOQ sample from rat plasma. The percentage coefficient of variation (CV (%)) for peak area ratio (analyte to internal standard) of six replicate injections was ≤5 %, which met the acceptance criteria. The retention time was within ±0.5 min variation in each analytical run.

Sample Preparation. Extraction of (*S*)-**7** and warfarin (internal standard) from samples of rat plasma was done by a protein precipitation (crashing) method. To a 20 μL aliquot of CC/QC/study samples, 20 μL of internal standard working solution was added to all the tubes except for the standard blank sample and vortexed. To the standard blank sample, 20 μL of diluent was added. To all the pre-labeled microcentrifuge tubes (1.5 mL capacity), 0.20 mL of acetonitrile was added for precipitation and vortexed (Vibramax 100, Heidolph Instruments) for about 10 min. The above samples were centrifuged (Eppendorf 5810R) for 10 min at 10,000 rpm and 4 °C. About 10 μL of the supernatant sample was injected for analysis into the SCIEX API 6500+ LC−MS/MS system.

Preparation of Calibration Standards and Quality Control Samples. The stock solutions of **(*S*)-7** and warfarin (internal standard) were prepared in dimethyl sulfoxide (DMSO) and acetonitrile at 1 mg/mL concentration, respectively. The stock solution of (*S*)-**7** was further diluted using DMSO to prepare calibration standard solutions in the concentration range of 20–40,000 ng/mL. For the internal standard, acetonitrile was used to prepare a working solution of concentration 500 ng/mL. These solutions were then spiked in interference-free rat blank plasma to obtain calibration standards in the pharmacologically relevant range (1–2000 ng/mL). Similarly, the quality control (QC) samples were prepared using independent stock solutions of analytes to obtain the concentrations of 4.00, 400, and 1000 ng/mL in rat plasma, representing low-, medium-, and high-concentration QC samples, respectively. The stock solutions, diluted standard solutions, quality control solutions, and internal standard solution were stored at 2−8 °C. The spiked plasma samples (calibration standards and quality controls) were prepared freshly prior to sample analysis.

Bioavailability Study of (S)-7 in Male Sprague−Dawley Rats. Sprague−Dawley rats for the study were obtained from Hylasco Biotechnology (India) Pvt., Ltd. (subsidiary of Charles River from USA). Animals were housed in polysulfonate cages with an enrichment device under typical research laboratory environments (temperature 25 ± 3 °C, relative humidity 50–70 %), with an approximately 12 h light/dark cycle. Altromin rat/mouse maintenance diets manufactured by Altromin

Spezialfutter GmbH, Germany, and charcoal-filtered water after UV ray treatment were used during the study. Experimentation on animals were approved by the Institutional Animal Ethics Committee and were in accordance with the Committee for the Purpose of Control and Supervision of Experiments on Animals (CPCSEA), Ministry of Social Justice and Environment, Government of India. All the rats were jugular vein cannulated and overnight fasted prior to dosing (except IV dose), and approximately 4 h post-dose food was offered to all animals. Formulations were made prior to dosing with test compound (*S*)-**7** and were maintained on continuous stirring during dosing. Compound (*S*)-**7** in 10 % DMSO + pH 7.4 PBS was used for IV administration, whereas 10 in 10 % DMSO +5 % Cremophor EL + 30 % PEG400 + 20 % PG + pH 7.4 PBS was used for PO administration. Animal weight on the day of dosing was used to calculate the required volume of formulation, which was administered to the rats accordingly. Test compound (*S*)-**7** at a dose of 1 mg/kg body weight was injected as IV bolus and at a dose of 5 mg/kg body weight administered orally. Blood samples at a volume of approximately 0.250 mL were collected from the jugular vein at 0.083 (IV only), 0.25, 0.5, 1, 2, 4, 6, 8, and 24 h post dose administration into prelabeled microcentrifuge tubes containing dipotassium ethylenediaminetetraacetic acid (K_2EDTA) anticoagulant at the final concentration of 4 mM. The blood samples, after mixing, were centrifuged at 2400 g for 10 min at a set temperature of 4 °C. The collected plasma samples were stored below −60 °C until bioanalysis. Pharmacokinetic parameters were calculated by a non-compartmental analysis tool of the validated Phoenix WinNonlin 8.3. Cmax, and Tmax, and exposures (AUClast and AUCinfinity) were calculated as applicable. Additionally, pharmacokinetic parameters for parenteral routes like C_0, elimination half-life ($T_{1/2}$), hepatic clearance (Cl), and distribution volume (V_d) were estimated. Absolute oral bioavailability (%F) was calculated with dose-normalized exposure of non-IV against dose-normalized IV exposure.

In Vivo Antihyperglycemic Screening: STZ-Induced Diabetic Mouse Model. Swiss Albino mice weighing about 13–34 g were used for animal studies. Experimental protocols were approved by the Institutional Animal Ethical Committee (No. 1972/PH/BIT/132/21/IAEC) of the Department of Pharmaceutical Sciences and Technology, Birla Institute of Technology, Mesra, Ranchi. All the experiments were conducted in accordance with the National Institutes of Health Guide for Care and Use of Laboratory Animals. Polypropylene cages containing wood shaving as bedding material were used for housing the experimental animals in six groups of five animals each. All the groups were maintained in the departmental animal house with a natural light/dark cycle at 26 ± 2 °C and 44−55 % relative humidity for 7 days [57]. All animals (except normoglycemic control, group 6) were rendered diabetic by the administration of STZ in 0.1 M citrate buffer (pH 4.5) at a dose of 40 mg/kg body weight (bw) for 5 consecutive days through an intraperitoneal route. Equal volume of citrate buffer was injected into normoglycemic control group mice. Drinking water was replaced with 10 % sucrose solution on days 4 and 5 except for normoglycemic control group, which received normal saline. Then, the animals were monitored for next 12 days for the development of diabetes. Mice were considered as diabetic if their blood glucose levels were above 250 mg/dL on days 10–12 after STZ administration. The normoglycemic control group received normal saline. Animals were grouped as follows: diabetic control (group 1), mice treated with 30 mg/kg pioglitazone bw (group 2), mice treated with 25 mg/kg bw (*S*)-**7** (group 3), mice treated with 50 mg/kg bw (*S*)-**7** (group 4), mice treated with 25 mg/kg bw (*S*)-**7** + pioglitazone (group 5), and normoglycemic control (group 6). Groups 2, 3, 4, and 5 received standard and test drugs as 0.25 % suspension in Tween 80 by oral route for 15 days. Blood glucose levels were determined from blood obtained from the tail vein of the animal on days 0, 5, 10, and 15, using a glucose meter (Contour Plus, Ascensia Diabetes Care Holdings AG). All animals had ad libitum access to food (rodent diet) and water before, during, and after the experiment.

Lipid Profiling of Compound (S)-7 in an STZ-Induced Diabetic Mouse Model. Before sacrificing the animals, blood samples were collected from the retro-orbital region under light anesthesia and were pooled group-wise for measurement of TC, high-density lipoprotein cholesterol (HDL), low-density lipoprotein cholesterol (LDL), very low-density lipoprotein cholesterol (VLDL), and TG. All these measurements were done by using commercially available kits (Span Diagnostic Ltd., Gujarat, India) in a clinical analyzer (RX 50V, Biochemistry Analyzer, Micro Lab, Gujarat, India).

Histopathological Study. Mice from each group were sacrificed under light anesthesia using diethyl ether. Bone, kidney, and liver tissues were dissected, washed in ice-cold physiological saline, fixed in a 15 % buffered neutral formalin solution, and, finally, embedded into paraffin blocks. Then, the tissue was sliced out into sections of 5 μm thickness by a rotator microtome and stained with hematoxylin−eosin. Obtained sections were examined by a Leica DME microscope, and representative photomicrographs were taken by a 7.1-megapixel Canon PowerShot S70 digital camera.

Statistical Analysis. Statistical analyses for data in vitro were performed using unpaired Student's T test or via one-way ANOVA analysis of variance with Dunnet post-test analysis for multiple group comparisons using GraphPad Prism version 8.3.0 (GraphPad Software, San Diego, CA). Differences with p values < 0.05 were considered statistically significant.

All statistical tests for data in vivo were performed using GraphPad Prism 5.0 software (San Diego, California, USA). Results were expressed as mean ± S.E.M. (standard error of the mean) for five rats in each group. The data was analyzed by one-way analysis of variance (ANOVA) followed by Dunnett's multiple-variance test. Differences were considered statistically significant at the levels of $p < 0.05$.

Accession codes

PDB codes of PPARα/(*S*)-**7** and PPARγ/(*S*)-**7** are 8RCE and 8REJ, respectively.

CRediT authorship contribution statement

Antonio Laghezza: Investigation. **Carmen Cerchia:** Investigation. **Massimo Genovese:** Investigation. **Roberta Montanari:** Investigation. **Davide Capelli:** Investigation. **Judith Wackerlig:** Investigation. **Stefan Simic:** Investigation. **Emanuele Falbo:** Investigation. **Lucia Pecora:** Investigation. **Rosalba Leuci:** Investigation. **Leonardo Brunetti:** Investigation. **Luca Piemontese:** Investigation. **Paolo Tortorella:** Funding acquisition. **Abanish Biswas:** Investigation. **Ravi Pratap Singh:** Investigation. **Suhas Tambe:** Investigation. **C.A. Sudeep:** Investigation. **Ashok Kumar Pattnaik:** Investigation. **Venkatesan Jayaprakash:** Investigation. **Paolo Paoli:** Writing – original draft, Investigation. **Antonio Lavecchia:** Writing – original draft, Investigation. **Fulvio Loiodice:** Writing – original draft, Conceptualization.

Declaration of competing interest

The authors declare that they have no known competing financial interests or personal relationships that could have appeared to influence the work reported in this paper.

Data availability

Data will be made available on request.

Acknowledgments

This work was accomplished thanks to the financial support of "European Union – Next Generation EU" (PRIN 2022, project number: 2022P5LPHS).

Supporting Information

Statistics of crystallographic data and refinement; superposition of *(S)*-**7** (cyan), LT175 and LJ570 within the PPARγ LBD; RMSD plot and summary of the interactions during MD simulation of (*S*)-**7** and Wy-14,643 within PPARγ and/or PPARα; overlay of the ternary complex of PPARγ LBD/(*S*)-**7**/**20** obtained after 100 ns MD simulation with the antagonist SR16832 or with ligands T2384 and S35 co-crystallized into PPARγ LBD; overlay of fenofibric acid co-crystallized into PPARα LBD in the presence of **20** with (*S*)-**7** pose obtained by docking and after 100 ns MD; overlay of Wy-14,643 pose into the **20**-bound PPARα LBD as predicted by docking and at the end of 100 ns MD simulation with its crystallographic pose. HPLC traces of enantiomers (*S*)-**7** and (*R*)-**7**.

Appendix A. Supplementary data

Supplementary data to this article can be found online at https://doi.org/10.1016/j.ejmech.2024.116567.

References

[1] B. Grygiel-Górniak, Peroxisome proliferator-activated receptors and their ligands: nutritional and clinical implications - a review, Nutr. J. 13 (2014) 17.

[2] A.S. Laganà, S.G. Vitale, A. Nigro, V. Sofo, F.M. Salmeri, P. Rossetti, A.M. C. Rapisarda, S. La Vignera, R.A. Condorelli, G. Rizzo, M. Buscema, Pleiotropic actions of peroxisome proliferator-activated receptors (PPARs) in dysregulated metabolic homeostasis, inflammation and cancer: current evidence and future perspectives, Int. J. Mol. Sci. 17 (2016) 999.

[3] G.S. Harmon, M.T. Lam, C.K. Glass, PPARs and lipid ligands in inflammation and metabolism, Chem. Rev. 111 (2011) 6321–6340.

[4] M.J. Chapman, H.N. Ginsberg, P. Amarenco, F. Andreotti, J. Borén, A.L. Catapano, O.S. Descamps, E. Fisher, P.T. Kovanen, J.A. Kuivenhoven, P. Lesnik, L. Masana, B. G. Nordestgaard, K.K. Ray, Z. Reiner, M.R. Taskinen, L. Tokgozoglu, A. Tybjærg-Hansen, G.F. Watts, European atherosclerosis society consensus panel. Triglyceride-rich lipoproteins and high-density lipoprotein cholesterol in patients at high risk of cardiovascular disease: evidence and guidance for management, Eur. Heart J. 32 (2011) 1345–1361.

[5] A. Keech, R.J. Simes, P. Barter, J. Best, R. Scott, M.R. Taskinen, P. Forder, A. Pillai, T. Davis, P. Glasziou, P. Drury, Y.A. Kesaniemi, D. Sullivan, D. Hunt, P. Colman, M. d'Emden, M. Whiting, C. Ehnholm, M. Laakso, Field Study Investigators. Effects of long-term fenofibrate therapy on cardiovascular events in 9795 people with type 2 diabetes mellitus (the FIELD study): randomised controlled trial, Lancet 366 (2005) 1849–1861.

[6] J.-C. Fruchart, Peroxisome proliferator-activated receptor-alpha (PPARalpha): at the crossroads of obesity, diabetes and cardiovascular disease, Atherosclerosis 205 (2009) 1–8.

[7] Y. Sasaki, M. Asahiyama, T. Tanaka, S. Yamamoto, K. Murakami, W. Pemafibrate Kamiya, A selective PPAR modulator, prevents non-alcoholic steatohepatitis development without reducing the hepatic triglyceride content, Sci. Rep. 10 (2020) 7818.

[8] A. Zieleniak, M. Wójcik, L.A. Woźniak, Structure and physiological functions of the human peroxisome proliferator-activated receptor gamma, Arch. Immunol. Ther. Exp. 56 (2008) 331–345.

[9] I.W. Campbell, The clinical significance of PPAR gamma agonism, Curr. Mol. Med. 5 (2005) 349–363.

[10] J.G. Neels, P.A. Grimaldi, Physiological functions of peroxisome proliferator-activated receptor β, Physiol. Rev. 94 (2014) 795–858.

[11] Study Group Accord, H.N. Ginsberg, M.B. Elam, L.C. Lovato, J.R. Crouse 3rd, L. A. Leiter, P. Linz, W.T. Friedewald, J.B. Buse, H.C. Gerstein, J. Probstfield, R. H. Grimm, F. Ismail-Beigi, J.T. Bigger, D.C. Goff Jr., W.C. Cushman, D.G. Simons-Morton, R.P. Byington, Effects of combination lipid therapy in type 2 diabetes mellitus, N. Engl. J. Med. 362 (2010) 1563–1574.

[12] Y. Guan, C. Hao, D.R. Cha, R. Rao, W. Lu, D.E. Kohan, M.A. Magnuson, R. Redha, Y. Zhang, M.D. Breyer, Thiazolidinediones expand body fluid volume through PPARγ stimulation of ENaC-mediated renal salt absorption, Nat. Med. 11 (2005) 861–866.

[13] P.D. Home, S.J. Pocock, H. Beck-Nielsen, P.S. Curtis, R. Gomis, M. Hanefeld, N. P. Jones, M. Komajda, J.J. McMurray, RECORD Study Team, Rosiglitazone evaluated for cardiovascular outcomes in oral agent combination therapy for type 2 diabetes (RECORD). A multicentre, randomised, open-label trial, Lancet 373 (2009) 2125–2135.

[14] K.R. Shockley, O.P. Lazarenko, P.J. Czernik, C.J. Rosen, G.A. Churchill, B. Lecka-Czernik, PPARγ2 nuclear receptor controls multiple regulatory pathways of osteoblast differentiation from marrow mesenchymal stem cells, J. Cell. Biochem. 106 (2009) 232–246.

[15] W. Wei, X. Wang, M. Yang, L.C. Smith, P.C. Dechow, J. Sonoda, R.M. Evans, Y. Wan, PGC1α mediates PPARγ activation of osteoclastogenesis and rosiglitazone-induced bone loss, Cell Metabol. 11 (2010) 503–516.

[16] A. Sosale, B. Saboo, B. Sosale, Saroglitazar for the treatment of hypertriglyceridemia in patients with type 2 diabetes: current evidence, Diabetes, Metab. Syndr. Obes. 8 (2015) 189–196.

[17] D.P. Kumar, R. Caffrey, J. Marioneaux, P.K. Santhekadur, M. Bhat, C. Alonso, The PPARα/γ agonist saroglitazar improves insulin resistance and steatohepatitis in a diet induced animal model of nonalcoholic fatty liver disease, Sci. Rep. 10 (2020) 9330.

[18] H.W. Lee, J.B. Ahn, S.K. Kang, S.K. Ahn, D.C. Ha, Process development and scale-up of PPARα/γ dual agonist lobeglitazone sulfate (CKD-501), Org. Process Res. Dev. 11 (2007) 190–199.

[19] H. Bae, T. Park, H. Kim, M. Lee, B.S. Cha, Lobeglitazone: a novel thiazolidinedione for the management of type 2 diabetes mellitus, Diabetes Metab. J. 45 (2021) 326–336.

[20] J. Weiping, J. Ma, H. Miao, C. Wang, X. Wang, Q. Li, W. Lu, J. Yang, L. Zhang, J. Yang, G. Wang, X. Zhang, M. Zhang, L. Sun, X. Yu, J. Du, B. Shi, C. Xiao, D. Zhu, H. Liu, L. Zhong, C. Xu, Q. Xu, G. Liang, Y. Zhang, G. Li, M. Gu, J. Liu, Z. Ning, L. Ji, 18-OR: efficacy and safety of chiglitazar vs. sitagliptin in patients with type 2 diabetes: a 24-week, randomized, double-blind, noninferiority phase 3 trial (CMAS), Diabetes 68 (Sup1) (2019) 18–OR.

[21] B. Boubia, O. Poupardin, M. Barth, J. Binet, P. Peralba, L. Mounier, E. Jacquier, E. Gauthier, V.r. Lepais, M. Chatar, Design, synthesis, and evaluation of a novel series of indole sulfonamide peroxisome proliferator activated receptor (PPAR) α/γ/δ triple activators: discovery of lanifibranor, a new antifibrotic clinical candidate, J. Med. Chem. 61 (2018) 2246–2265.

[22] S.M. Francque, P. Bedossa, V. Ratziu, Q.M. Anstee, E. Bugianesi, A.J. Sanyal, R. Loomba, S.A. Harrison, R. Balabanska, L. Mateva, N. Lanthier, N. Alkhouri, C. Moreno, J.M. Schattenberg, D. Stefanova-Petrova, L. Vonghia, R. Rouzier, M. Guillaume, A. Hodge, M. Romero-Gómez, P. Huot-Marchand, M. Baudin, M. P. Richard, J.L. Abitbol, P. Broqua, J.L. Junien, M.F. Abdelmalek, A randomized, controlled trial of the pan-PPAR agonist lanifibranor in NASH, N. Engl. J. Med. 385 (2021) 1547–1558.

[23] D. Capelli, C. Cerchia, R. Montanari, F. Loiodice, P. Tortorella, A. Laghezza, L. Cervoni, G. Pochetti, A. Lavecchia, Structural basis for PPAR partial or full activation revealed by a novel ligand binding mode, Sci. Rep. 6 (2016) 34792.

[24] G. Pochetti, N. Mitro, A. Lavecchia, F. Gilardi, N. Besker, E. Scotti, M. Aschi, N. Re, G. Fracchiolla, A. Laghezza, P. Tortorella, R. Montanari, E. Novellino, F. Mazza, M. Crestani, F. Loiodice, Structural insight into peroxisome proliferator-activated receptor γ binding of two ureidofibrate-like enantiomers by molecular dynamics, cofactor interaction analysis, and site-directed mutagenesis, J. Med. Chem. 53 (2010) 4354–4366.

[25] M. Winitz, L.B. Frankenthal, N. Izumiya, S.M. Birnbaum, C.G. Baker, J. P. Greenstein, Studies on diastereoisomeric α-amino acids and corresponding α-hydroxy acids. VII. Influence of β-configuration on enzymic susceptibility, J. Am. Chem. Soc. 78 (1956) 2423–2430.

[26] a) A. Pinelli, C. Godio, A. Laghezza, N. Mitro, G. Fracchiolla, V. Tortorella, A. Lavecchia, E. Novellino, J.-C. Fruchart, B. Staels, M. Crestani, F. Loiodice, Synthesis, biological evaluation, and molecular modeling investigation of new chiral fibrates with PPARalpha and PPARgamma agonist activity, J. Med. Chem. 48 (2005) 5509–5519;
b) B. De Filippis, P. Linciano, A. Ammazzalorso, C. Di Giovanni, M. Fantacuzzi, L. Giampietro, A. Laghezza, C. Maccallini, P. Tortorella, A. Lavecchia, F. Loiodice, R. Amoroso, Structural development studies of PPARs ligands based on tyrosine scaffold, Eur. J. Med. Chem. 89 (2015) 817–825.

[27] R. Montanari, F. Saccoccia, E. Scotti, M. Crestani, C. Godio, F. Gilardi, F. Loiodice, G. Fracchiolla, A. Laghezza, P. Tortorella, A. Lavecchia, E. Novellino, F. Mazza, M. Aschi, G. Pochetti, Crystal structure of the peroxisome proliferator-activated receptor (PPARγ) ligand binding domain complexed with a novel partial agonist: a new region of the hydrophobic pocket could be exploited for drug design, J. Med. Chem. 51 (2008) 7768–7776.

[28] A. Laghezza, L. Piemontese, C. Cerchia, R. Montanari, D. Capelli, M. Giudici, M. Crestani, P. Tortorella, F. Peiretti, G. Pochetti, A. Lavecchia, F. Loiodice, Identification of the first PPARα/γ dual agonist able to bind to canonical and alternative sites of PPAR and to inhibit its Cdk5-mediated phosphorylation, J. Med. Chem. 61 (2018) 8282–8298.

[29] L.M. Leesnitzer, D.J. Parks, R.K. Bledsoe, J.E. Cobb, J.L. Collins, T.G. Consler, R. G. Davis, E.A. Hull-Ryde, J.M. Lenhard, L. Patel, K.D. Plunket, J.L. Shenk, J. B. Stimmel, C. Therapontos, T.M. Willson, S.G. Blanchard, Functional consequences of cysteine modification in the ligand binding sites of peroxisome proliferator activated receptors by GW9662, Biochemistry 41 (2002) 6640–6650.

[30] T.S. Hughes, P.K. Giri, I.M. de Vera, D.P. Marciano, D.S. Kuruvilla, Y. Shin, A. L. Blayo, T.M. Kamenecka, T.P. Burris, P.R. Griffin, D.J. Kojetin, An alternate binding site for PPARγ ligands, Nat. Commun. 5 (2014) 3571.

[31] I.A. Leijten-van de Gevel, K.H.N. van Herk, R.M.J.M. de Vries, N.J. Ottenheym, C. Ottmann, L. Brunsveld, Indazole MRL-871 interacts with PPARγ via a binding mode that induces partial agonism, Bioorg. Med. Chem. 68 (2022) 116877.

[32] R. Brust, H. Lin, J. Fuhrmann, A. Asteian, T.M. Kamenecka, D.J. Kojetin, Modification of the orthosteric PPARγ covalent antagonist scaffold yields an improved dual-site allosteric inhibitor, ACS Chem. Biol. 12 (2017) 969–978.

[33] a) R.A. Friesner, J.L. Banks, R.B. Murphy, T.A. Halgren, J.J. Klicic, D.T. Mainz, M. P. Repasky, E.H. Knoll, M. Shelley, J.K. Perry, D.E. Shaw, P. Francis, P.S. Shenkin, Glide: a new approach for rapid, accurate docking and scoring. 1. Method and assessment of docking accuracy, J. Med. Chem. 47 (2004) 1739–1749;
b) T.A. Halgren, R.B. Murphy, R.A. Friesner, H.S. Beard, L.L. Frye, W.T. Pollard, J. L. Banks, Glide: a new approach for rapid, accurate docking and scoring. 2. Enrichment factors in database screening, J. Med. Chem. 47 (2004) 1750–1759.

[34] J. Shang, R. Brust, S.A. Mosure, J. Bass, P. Munoz-Tello, H. Lin, T.S. Hughes, M. Tang, Q. Ge, T.M. Kamenekca, D.J. Kojetin, Cooperative cobinding of synthetic and natural ligands to the nuclear receptor PPARγ, Elife 7 (2018) e43320.
[35] T.S. Hughes, J. Shang, R. Brust, I.M.S. de Vera, J. Fuhrmann, C. Ruiz, M. D. Cameron, T.M. Kamenecka, D.J. Kojetin, Probing the complex binding modes of the PPARγ partial agonist 2-chloro-N-(3-chloro-4-((5-chlorobenzo[d]thiazol-2-yl) thio)phenyl)-4-(trifluoromethyl)benzenesulfonamide (T2384) to orthosteric and allosteric sites with NMR spectroscopy, J. Med. Chem. 59 (2016) 10335–10341.
[36] Y. Li, Z. Wang, N. Furukawa, P. Escaron, J. Weiszmann, G. Lee, M. Lindstrom, J. Liu, X. Liu, H. Xu, O. Plotnikova, V. Prasad, N. Walker, R.M. Learned, J.-L. Chen, T2384, a novel antidiabetic agent with unique peroxisome proliferator-activated receptor gamma binding properties, J. Biol. Chem. 283 (2008) 9168–9176.
[37] J.Y. Jang, M. Koh, H. Bae, D.R. An, H.N. Im, H.S. Kim, J.Y. Yoon, H.-J. Yoon, B. W. Han, S.B. Park, S.W. Suh, Structural basis for differential activities of enantiomeric PPARγ agonists: binding of S35 to the alternate site, Biochim. Biophys. Acta, Proteins Proteomics 1865 (2017) 674–681.
[38] H. Bae, J.Y. Jang, S.-S. Choi, J.-J. Lee, H. Kim, A. Jo, K.-J. Lee, J.H. Choi, S.W. Suh, S.B. Park, Mechanistic elucidation guided by covalent inhibitors for the development of anti-diabetic PPARγ ligands, Chem. Sci. 7 (2016) 5523–5529.
[39] J.B. Bruning, M.J. Chalmers, S. Prasad, S.A. Busby, T.M. Kamenecka, Y. He, K. W. Nettles, P.R. Griffin, Partial agonists activate PPARgamma using a helix 12 independent mechanism, Structure 15 (2007) 1258–1271.
[40] K.J. Bowers, E. Chow, H. Xu, R.O. Dror, M.P. Eastwood, B.A. Gregersen, J. L. Klepeis, I. Kolossvary, M.A. Moraes, F.D. Sacerdoti, J.K. Salmon, Y. Shan, D. E. Shaw, Scalable algorithms for molecular dynamics simulations on commodity clusters, in: Proceedings of the ACM/IEEE Conference on Supercomputing (SC06), Tampa, Florida, 2006 November 11-17.
[41] S. Kamata, T. Oyama, K. Saito, A. Honda, Y. Yamamoto, K. Suda, R. Ishikawa, T. Itoh, Y. Watanabe, T. Shibata, K. Uchida, M. Suematsu, I. Ishii, PPARα ligand-binding domain structures with endogenous fatty acids and fibrates, iScience 23 (2020) 101727.
[42] A.S. Divakaruni, S.E. Wiley, G.W. Rogers, A.Y. Andreyev, S. Petrosyan, M. Loviscach, E.A. Wall, N. Yadava, A.P. Heuck, D.A. Ferrick, R.R. Henry, W. G. McDonald, J.R. Colca, M.I. Simon, T.P. Ciaraldi, A.N. Murphy, Thiazolidinediones are acute, specific inhibitors of the mitochondrial pyruvate carrier, Proc. Ntl. Acad. Sci. USA 110 (2013) 5422–5427.
[43] A. Laghezza, C. Cerchia, M. Genovese, R. Leuci, E. Pranzini, A. Santi, L. Brunetti, L. Piemontese, P. Tortorella, A. Biswas, R.P. Singh, S. Tambe, S. Ca, A.K. Pattnaik, V. Jayaprakash, P. Paoli, A. Lavecchia, F. Loiodice, A new antidiabetic agent showing short- and long-term effects due to peroxisome proliferator-activated receptor alpha/gamma dual agonism and mitochondrial pyruvate carrier inhibition, J. Med. Chem. 66 (2023) 3566–3587.
[44] D.E.V. Pires, T.L. Blundell, D.B. Ascher, pkCSM: predicting small-molecule pharmacokinetic and toxicity properties using graph-based signatures, J. Med. Chem. 58 (2015) 4066–4072.
[45] Y. Guan, C. Hao, D.R. Cha, R. Rao, W. Lu, D.E. Kohan, M.A. Magnuson, R. Redha, Y. Zhang, M.D. Breyer, Thiazolidinediones expand body fluid volume through PPARγ stimulation of ENaC-mediated renal salt absorption, Nat. Med. 11 (2005) 861–866.
[46] W. Wei, X. Wang, M. Yang, L.C. Smith, P.C. Dechow, J. Sonoda, R.M. Evans, Y. Wan, PGC1β mediates PPARγ activation of osteoclastogenesis and rosiglitazone-induced bone loss, Cell Metabol. 11 (2010) 503–516.
[47] J. Zangari, F. Petrelli, B. Maillot, J.C. Martinou, The multifaceted pyruvate metabolism: role of the mitochondrial pyruvate carrier, Biomolecules 10 (2020) 1068.
[48] K.S. McCommis, Z. Chen, X. Fu, W.G. McDonald, J.R. Colca, R.F. Kletzien, S. C. Burgess, B.N. Finck, Loss of mitochondrial pyruvate carrier 2 in the liver leads to defects in gluconeogenesis and compensation via pyruvate-alanine cycling, Cell Metabol. 22 (2015) 682–694.
[49] D. Capelli, G. Cazzaniga, M. Mori, A. Laghezza, F. Loiodice, M. Quaglia, E. Negro, F. Meneghetti, S. Villa, R. Montanari, Biological screening and crystallographic studies of hydroxy-lactone derivatives to investigate PPARγ phosphorylation inhibition, Biomolecules 13 (2023) 694.
[50] C. Vonrhein, C. Flensburg, P. Keller, A. Sharff, O. Smart, W. Paciorek, T. Womack, G. Bricogne, Data processing and analysis with the autoPROC toolbox, Acta Crystallogr. D67 (2011) 293–302.
[51] J. Navaza, AMoRe: an automated package for molecular replacement, Acta Crystallogr. A50 (1994) 157–163.
[52] a) A.T. Brunger, P.D. Adams, G.M. Clore, W.L. Delano, P. Gros, R. W. Grossekunstleve, J.S. Jiang, J. Kuszewski, M. Nilges, N.S. Pannu, R.J. Read, L. M. Rice, T. Simonson, G.L. Warren, Crystallography & NMR system: a new software suite for macromolecular structure determination, Acta Crystallogr. D54 (1998) 905–921;
b) A.T. Brunger, Version 1.2 of the crystallography and NMR system, Nat. Protoc. 2 (2007) 2728–2733.
[53] W.X.D.S. Kabsch, Acta Crystallogr. D66 (2010) 125–132.
[54] R. Torices, A.J. Muñoz-Pajares, PHENIX: an R package to estimate a size-controlled phenotypic integration index, Appl. Plant Sci. 3 (2015) 1400104.
[55] C. Lu, C. Wu, D. Ghoreishi, W. Chen, L. Wang, W. Damm, G.A. Ross, M.K. Dahlgren, E. Russell, C.D. Von Bargen, R. Abel, R.A. Friesner, E.D. Harder, OPLS4: improving force field accuracy on challenging regimes of chemical space, J. Chem. Theor. Comput. 17 (2021) 4291–4300.
[56] T. Hollon, F.K. Yoshimura, Variation in enzymatic transient gene expression assays, Anal. Biochem. 182 (1989) 411–418.
[57] S. Yasmin, F. Capone, A. Laghezza, F.D. Piaz, F. Loiodice, V. Vijayan, V. Devadasan, S.K. Mondal, Ö. Atlı, M. Baysal, A.K. Pattnaik, V. Jayaprakash, A. Lavecchia, Novel benzylidene thiazolidinedione derivatives as partial PPARγ agonists and their antidiabetic effects on type 2 diabetes, Sci. Rep. 7 (2017) 14453.

Update

European Journal of Medicinal Chemistry
Volume 287, Issue , 5 April 2025, Page

DOI: https://doi.org/10.1016/j.ejmech.2025.117375

European Journal of Medicinal Chemistry 287 (2025) 117375

Contents lists available at ScienceDirect

European Journal of Medicinal Chemistry

journal homepage: www.elsevier.com/locate/ejmech

Corrigendum to "A chemical modification of a peroxisome proliferator-activated receptor pan agonist produced a shift to a new dual alpha/gamma partial agonist endowed with mitochondrial pyruvate carrier inhibition and antidiabetic properties" [Eur. J. Med. Chem. 275 (2024) 116567]

Antonio Laghezza [a], Carmen Cerchia [b], Massimo Genovese [c], Roberta Montanari [d], Davide Capelli [d], Judith Wackerlig [e], Stefan Simic [e], Emanuele Falbo [b], Lucia Pecora [c], Rosalba Leuci [a], Leonardo Brunetti [a], Luca Piemontese [a], Paolo Tortorella [a], Abanish Biswas [f], Ravi Pratap Singh [f], Suhas Tambe [g], C.A. Sudeep [h], Ashok Kumar Pattnaik [f], Venkatesan Jayaprakash [f], Paolo Paoli [c], Antonio Lavecchia [b,**], Fulvio Loiodice [a,*]

[a] *Dipartimento Farmacia-Scienze del Farmaco, Universita' degli Studi di Bari "Aldo Moro", via Orabona 4, 70125, Bari, Italy*
[b] *Dipartimento di Farmacia, "Drug Discovery" Laboratory, Universita' degli Studi di Napoli "Federico II", via D. Montesano 49, 80131, Napoli, Italy*
[c] *Dipartimento di Scienze Biomediche Sperimentali e Cliniche, Sezione di Scienze Biochimiche, Universita' degli Studi di Firenze, Viale Morgagni 50, 50134, Firenze, Italy*
[d] *Istituto di Cristallografia, Consiglio Nazionale delle Ricerche, Montelibretti, 00015 Monterotondo Stazione, Roma, Italy*
[e] *Department of Pharmaceutical Sciences, Faculty of Life Sciences, University of Vienna, 1090, Vienna, Austria*
[f] *Department of Pharmaceutical Sciences & Technology, Birla Institute of Technology, Mesra, Ranchi, Jharkhand, 835215, India*
[g] *Adgyl Lifescience Private Ltd., Bengaluru, 560058, India*
[h] *Bioanalytical Section, Eurofins Advinus Biopharma Services India Pvt Ltd., Bengaluru, 560058, India*

The authors regret.

Acknowledgments:This work was accomplished thanks to the financial support of "European Union – Next Generation EU" (PRIN 2022, project number: 2022P5LPHS). We acknowledge the European Synchrotron Radiation Facility for provision of synchrotron radiation facilities and we would like to thank David Flot for assistance in using beamline 30.

The authors would like to apologise for any inconvenience caused.

DOI of original article: https://doi.org/10.1016/j.ejmech.2024.116567.
* Corresponding author. Dipartimento di Farmacia-Scienze del Farmaco, Universita' degli Studi di Bari "Aldo Moro", Via E. Orabona 4, 70125, Bari, Italy.
** Corresponding author.
E-mail address: fulvio.loiodice@uniba.it (F. Loiodice).

https://doi.org/10.1016/j.ejmech.2025.117375

Available online 12 February 2025